

Flux of Atmospheric Neutrinos*

T.K. Gaisser¹ and M. Honda²

¹Bartol Research Institute, University of Delaware, Newark, DE 19716 USA;

²Institute for Cosmic Ray Research, University of Tokyo, 5-1-5 Kashiwanoha Kashiwa-shi,
Chiba 277-8582, Japan

KEYWORDS: atmospheric muons and neutrinos, cosmic rays, neutrino oscillations, neutrino
astronomy

ABSTRACT: Atmospheric neutrinos produced by cosmic-ray interactions in the atmosphere are of interest for several reasons. As a beam for studies of neutrino oscillations they cover a range of parameter space hitherto unexplored by accelerator neutrino beams. The atmospheric neutrinos also constitute an important background and calibration beam for neutrino astronomy and for the search for proton decay and other rare processes. Here we review the literature on calculations of atmospheric neutrinos over the full range of energy, but with particular attention to the aspects important for neutrino oscillations. Our goal is to assess how well the properties of atmospheric neutrinos are known at present.

CONTENTS

Introduction	3
Overview of Neutrino Flux Calculations	8

*With permission from the Annual Review of Nuclear & Particle Science. Final version of this material is scheduled to appear in the Annual Review of Nuclear & Particle Science Vol. 52, to be published in December 2002 by Annual Reviews (<http://annualreviews.org>).

<i>Early calculations</i>	9
<i>Analytic approximations</i>	12
<i>Response functions</i>	15
Primary Spectrum	16
<i>Summary of data on protons and helium</i>	17
<i>Heavier nuclei and the all-nucleon spectrum</i>	19
<i>Solar modulation</i>	20
Geomagnetic effects	23
<i>Cutoffs for realistic magnetic field</i>	24
<i>East-West Effect</i>	27
<i>Second (subcutoff) spectrum</i>	29
Hadronic interactions	31
<i>Cross sections</i>	32
<i>Pion and kaon production by protons</i>	35
<i>High energies</i>	37
Comparison of neutrino flux calculations	39
Three-dimensional calculations	42
<i>Geometry of neutrino production</i>	44
<i>Pathlength distributions</i>	49
Atmospheric muons	51
Uncertainties in the Calculated Neutrino Fluxes	55
<i>Uncertainties from primary spectrum</i>	56
<i>Uncertainties from hadronic interactions</i>	56
<i>Other sources of uncertainty</i>	57
<i>Comparison to measurements</i>	57

Global view of the neutrino spectrum	60
Acknowledgments	61
LITERATURE CITED	61

1 Introduction

When primary cosmic-ray protons and nuclei enter the atmosphere their interactions produce secondary, “atmospheric” cosmic rays including all the hadrons and their decay products. The spectrum of these secondaries peaks in the GeV range, but extends to high energy with approximately a power-law spectrum. Because they are weakly interacting, neutrinos were the last component of the secondary cosmic radiation to be studied, and the time-scale for progress has been correspondingly slow. The basic principles of detection and very rough estimates of rates were known by 1960. Markov (1) suggested the idea of detecting neutrino-induced horizontal or upward-moving muons in a detector in a deep body of water and estimated the rates that might be observed (2). Greisen (3) estimated roughly the rate of neutrino interactions inside a large, deep Cherenkov detector. Two groups (4, 5) independently reported observations of atmospheric neutrinos in 1965 by detecting horizontal muons in detectors so deep that the muons could not have been produced in the atmosphere.

With the advent of very large, deep underground detectors, whose construction was originally motivated by the search for proton decay, there are now extensive measurements of the flux of atmospheric neutrinos in which the events occur within the fiducial volume of the detector. What is emerging from recent studies is a discovery which is likely to have an impact comparable to that of the discoveries

made with atmospheric cosmic rays half a century ago, including existence of the pion, the kaon and the muon. The 50 kiloton SuperKamiokande experiment, with a 20 kiloton fiducial volume, has now accumulated sufficient statistics to see clearly that the flux of muon-neutrinos depends not only on the rate at which they are produced in the atmosphere, but also on the pathlength they travel to the detector (6).

The detector has a cylindrical shape, and its response is up-down symmetric to within a few percent. The atmospheric neutrino beam is also symmetric under reflection about a horizontal plane through the detector—except for geomagnetic effects that we discuss in detail below. There is nevertheless a deficit of upward muon-neutrinos, with pathlengths of order 10^4 km, relative to downward neutrinos, which are produced within tens of kilometers of the detector.

The most likely cause of this pathlength-dependence is neutrino oscillations, in which neutrinos produced as muon-type, after passing a certain distance (which depends on energy), manifest themselves with a different “flavor”, in this case as ν_τ (7). The implication of this behaviour is that the neutrinos possess a small but non-zero mass, thus pointing to physics beyond the standard model of particle physics. This discovery has stimulated intense activity to find the implications for particle theory, and to relate this manifestation of neutrino physics to the solar neutrino problem, which is now also understood to be another manifestation of neutrino properties (8).

The first evidence that atmospheric neutrinos were not behaving as expected came from the observation by IMB that the fraction of neutrino interactions with stopping muons was lower than expected (9). Then Kamioka reported that the ratio of muon-like to electron-like neutrino interactions was lower than ex-

pected (10). The Frejus experiment, however, reported a ratio consistent with expectation (11). These detectors had fiducial volumes ranging from a fraction to a few kilotons. As statistics accumulated from the water detectors (IMB and Kamioka) (12, 13, 14, 15) and results were reported from Soudan (16), evidence for the *atmospheric neutrino anomaly* increased. In the last paper from the Kamioka experiment (17), the first evidence for a pathlength dependence characteristic of neutrino oscillations emerged.

In the case of mixing between two flavors of neutrinos, one of which is ν_μ , the probability that a neutrino produced as a ν_μ travels a distance L and is detected as a ν_μ is

$$P_{\nu_\mu \rightarrow \nu_\mu} = 1 - \sin^2(2\theta_m) \sin^2 \left[1.27 \delta m^2 \frac{L_{km}}{E_{GeV}} \right], \quad (1)$$

where $\delta m^2 = m_1^2 - m_2^2$ is the difference of the squared masses of the two related mass eigenstates and θ_m is the angle that characterizes mixing between the two states. Thus the characteristic signature of neutrino oscillations is a deviation from the expected flux as L/E varies. Currently, the best fit to the data of Super-K (7) has $\delta m^2 \approx 3.2 \times 10^{-3} \text{ eV}^2$ with full mixing, $\theta_m \approx \pi/4$.

Fig. 1 summarizes the current situation with the measurements of Super-K. One sees that the characteristic first oscillation dip cannot be resolved at present with Super-Kamiokande. This is a consequence of its limited energy and angular resolution coupled with the fact that, with the estimated value of δm^2 , the first minimum occurs for pathlengths

$$L \approx 400 \text{ km} \times E_\nu(\text{GeV}). \quad (2)$$

This distance from production in the atmosphere to underground detector corresponds to neutrinos coming from near the horizon where the pathlength changes rapidly with zenith angle. This consideration (18) limits the accuracy with which

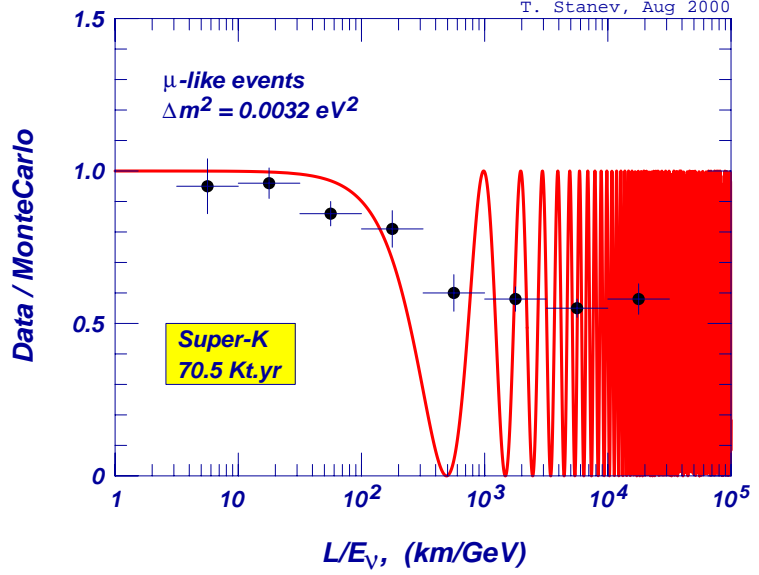


Figure 1: Oscillation probability as a function of L/E_ν .

δm^2 can be determined with the atmospheric neutrino beam. On the other hand (18) the determination of the value of the mixing angle, since it is large, can be very precise with atmospheric neutrinos, limited only by statistics.

Contained neutrino events in Super-Kamiokande are classified as sub-GeV and multi-GeV. To probe the atmospheric neutrino spectrum at higher energy it is necessary to make use the older technique of neutrino-induced muons, where the effective volume is the projected area of the detector times the muon range. Since the muon range increases with energy, so does the effective volume. Fig. 2 shows the distribution of neutrino energies for four classes of events. The $\nu_\mu \leftrightarrow \nu_\tau$ oscillation interpretation that is emerging from the data is also consistent with deviations from the expected angular distributions of neutrino-induced upward muons measured in MACRO (19) and Super-Kamiokande (20) and with the ratios of stopping to throughgoing upward muons (21, 22).

The experimental evidence for oscillations of atmospheric neutrinos is the subject to two recent reviews (23, 24). Here we focus on calculations of the at-

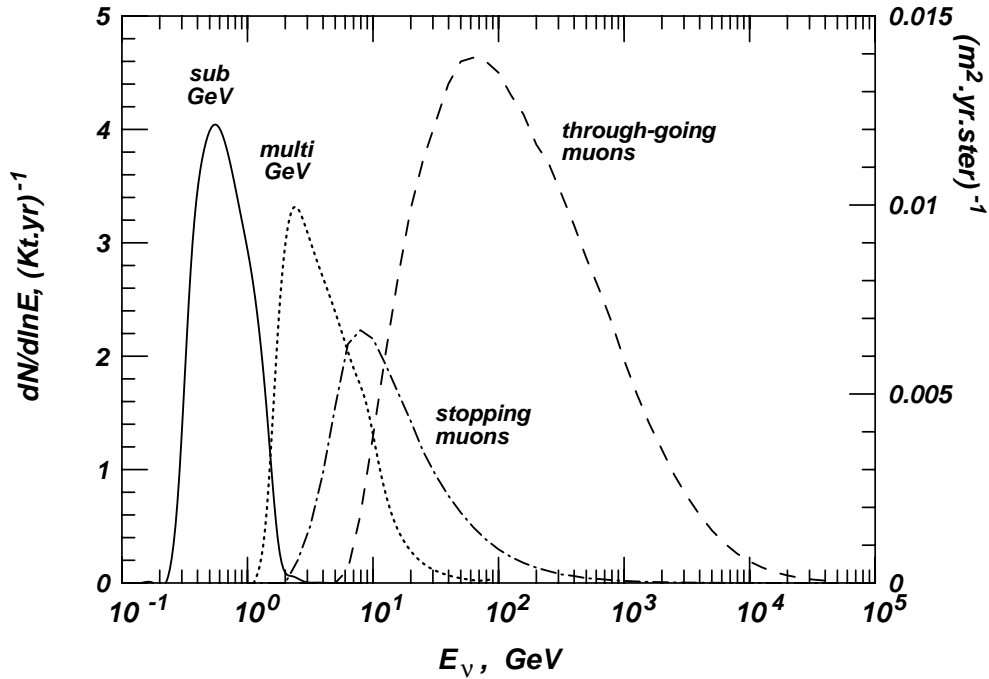


Figure 2: Distributions of neutrino energies that give rise to four classes of events. Sub-GeV and multi-GeV refer to the two classes of contained events at Superkamiokande. Stopping and throughgoing muons refer respectively to neutrino-induced muons produced outside the detector.

atmospheric neutrino flux. In doing so, we will emphasize those aspects that are important for making inferences about oscillations. These include the flavor ratios and angular distributions as well as pathlength distributions as a function of angle.

We will also discuss the absolute normalization of the flux and the energy spectra up to very high energy. While inferences about oscillations emphasize measurements of ratios to minimize their dependence on the absolute accuracy of atmospheric neutrino flux calculations, the normalization is still important for checking the overall consistency of the measurements and calculations. In

addition, high energy atmospheric neutrinos constitute the background for neutrino astronomy at all energies. Both Baikal (25) and AMANDA (26) have detected atmospheric neutrinos. Neutrino telescopes with larger effective volume are planned (27, 28, 29, 30). More important is that the atmospheric neutrinos will be the primary calibration beam for the neutrino telescopes.

We organize the review as follows. After giving an overview of the calculations in §2, in the next three sections we review the primary spectrum, geomagnetic effects and hadronic interactions, which are the principal physical quantities that influence the neutrino spectrum. Then in §6 we turn to a comparison of different calculations. Until recently, nearly all calculations were one-dimensional in the sense that all secondaries were assumed to follow the direction of the parent cosmic-ray from which they descended. In §7 we review the novel features of the recent three-dimensional calculations. Atmospheric muons are closely related to atmospheric neutrinos, and they therefore provide an essential constraint. We review the muon data in relation to the neutrinos in §8. In §9 we enumerate the uncertainties in the various ingredients of the calculations and estimate the resulting uncertainty in the atmospheric neutrino flux.

2 Overview of Neutrino Flux Calculations

The atmospheric neutrino flux is a convolution of the primary spectrum at the top of the atmosphere with the yield (Y) of neutrinos per primary particle. To reach the atmosphere and interact, the primary cosmic rays first have to pass through the geomagnetic field. Thus the flux of neutrinos of type i can be represented as

$$\phi_{\nu_i} = \phi_p \otimes R_p \otimes Y_{p \rightarrow \nu_i} + \sum_A \{ \phi_A \otimes R_A \otimes Y_{A \rightarrow \nu_i} \}, \quad (3)$$

where $\phi_{p(A)}$ is the flux of primary protons (nuclei of mass A) outside the influence of the geomagnetic field and $R_{p(A)}$ represents the filtering effect of the geomagnetic field. Free and bound nucleons are treated separately because propagation through the geomagnetic field depends on magnetic rigidity (total momentum divided by total charge) whereas particle production depends to a good approximation on energy per nucleon. A proton of rigidity R (GV) has total energy per nucleon $E(\text{GeV}) = \sqrt{R^2 + m_p^2}$ whereas the corresponding relation for helium is $E(\text{GeV}/A) = \sqrt{R^2/4 + m_p^2}$.

The neutrinos come primarily from the two-body decay modes of pions and kaons and the subsequent muon decays. The decay chain from pions is

$$\begin{aligned} \pi^\pm &\rightarrow \mu^\pm + \nu_\mu(\bar{\nu}_\mu) \\ &\searrow \\ &e^\pm + \nu_e(\bar{\nu}_e) + \bar{\nu}_\mu(\nu_\mu), \end{aligned} \tag{4}$$

with a similar chain for charged kaons. When conditions are such that all particles decay, we therefore expect

$$\begin{aligned} \frac{\nu_\mu + \bar{\nu}_\mu}{\nu_e + \bar{\nu}_e} &\sim 2, \\ \nu_\mu/\bar{\nu}_\mu &\sim 1 \quad \text{and} \quad \nu_e/\bar{\nu}_e \sim \mu^+/\mu^-. \end{aligned} \tag{5}$$

Moreover, the kinematics of π and μ decay is such that roughly equal energy is carried on average by each neutrino in the chain.

2.1 Early calculations

The early calculations used the relation between muons and neutrinos implied by Eq. 4. The idea is to parameterize the pion production spectrum in the atmosphere to fit an observed flux of muons. In this way, the primary spectrum

and the particle production do not enter the calculation of the neutrino flux explicitly. Since the kinematical relation between neutrinos and their parent pions is different for pions and kaons, some assumption about their relative importance has to be made.

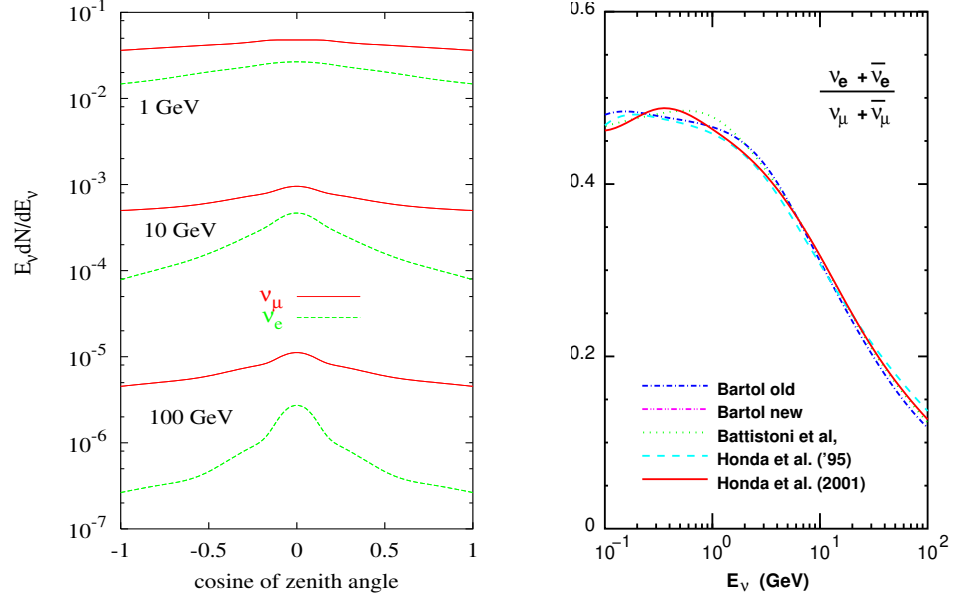


Figure 3: Left panel: Zenith-angle dependence of $\nu + \bar{\nu}$ calculated in the absence of a geomagnetic field. Right panel: Ratio of $(\nu_e + \bar{\nu}_e)/(\nu_\mu + \bar{\nu}_\mu)$ as calculated in several recent papers including the geomagnetic field for the location of Super-Kamiokande (see §6).

Most of the essential features of the atmospheric neutrino spectrum were already displayed and discussed in the 1961 paper of Zatsepin and Kuz'min (31). Muons with energy of several GeV and above reach the ground before decaying, so the ν_e/ν_μ ratio decreases with increasing energy. The resulting steepening of the ν_e spectrum occurs at lower energy near the vertical direction and at higher energy near the horizon because of the longer decay path for the parent muons with large zenith angle. The component of the ν_μ flux from muon decay be-

haves the same way. For $E_\nu > 100/\cos\theta$ GeV, the ratio of electron to muon neutrinos approaches a small value $\lesssim 5\%$, with the main source of ν_e the decay $K_L^0 \rightarrow \pi e \nu_e$. To the extent that there is uncertainty in kaon production, there will be a corresponding uncertainty in this ratio at high energy. These features of the neutrino flux are illustrated in Fig. 3. The left panel shows the neutrino fluxes from Ref. (32) calculated in the artificial case of no geomagnetic cutoff and shown as a function of cosine of the zenith angle. The right panel shows the key ratio of electron neutrinos to muon neutrinos from several calculations (32, 33, 34, 35, 36) averaged over all directions for the specific location of Super-K.

In calculating neutrinos from decay of muons, it is important to include the effect of muon polarization. Although they did not include it in their calculation, Zatsepin and Kuz'min pointed out that it would have the effect of increasing the ν_e/ν_μ ratio by about 5%. Muons are produced fully polarized in the two-body decays of pions and kaons, with the direction of polarization determined by the direction of the muon in the rest frame of its parent. Because of the steep spectrum, the effect does not average to zero in the integral over the parent energies. Moreover, it has the same sign for neutrinos and antineutrinos. Volkova (37) pointed out the importance of neutrino polarization in the context of the atmospheric neutrino anomaly.

The angular and energy dependence of muons and neutrinos from decay of pions and kaons is determined by the competition between decay and interaction of the parent mesons. The critical energy for pions in the atmosphere is $\epsilon_\pi \approx 115$ GeV, and $\epsilon_K \approx 850$ GeV for kaons. For $E_\nu \ll \epsilon/\cos\theta$ the neutrino spectrum has approximately the same power as the parent meson production spectrum and hence of the primary spectrum of nucleons. For $E_\nu \gg \epsilon \cos\theta$ the neutrino

spectrum is one power steeper and is proportional to $\sec(\theta)$. Since $\epsilon_K > \epsilon_\pi$, the spectrum of neutrinos from pion decay steepens before that of neutrinos from decay of kaons, so that kaons become increasingly important at high energy. Since the change of slope depends on zenith angle as well as energy, it is possible in principle to use the observed (E, θ) dependence of the muon flux to estimate, or at least set an upper limit, on the fraction of kaons. Ref. (38) used this method to show that atmospheric muons are not dominated by kaons.

The importance of kaons relative to pions is further enhanced at high energies for neutrinos as compared to muons because most of the energy in pion decay goes to the muon as compared to the neutrino, whereas it is divided nearly equally in the $K \rightarrow \mu\nu$ decay. For $E_\nu > 100$ GeV kaons become the dominant source of neutrinos even though the kaon/pion ratio at production is small.

Perkins (39, 40) has reviewed calculations that reconstruct the neutrino flux from the muon flux. Refinements account for variation of the geomagnetic field over the globe and start from muon data at high altitude where most of the pion and kaon decays occur. Recent calculations, however, use the method of Eq. 3, which is amenable to detailed monte carlo simulations, and we will concentrate on those results in this review.

2.2 Analytic approximations

Before proceeding to the details of the review, it will be helpful to discuss briefly the analytic approximations for the neutrino flux as a guide to the physics of atmospheric neutrinos. Not only do these approximations allow a good qualitative understanding of the features of the atmospheric neutrino flux, but they are valuable for diagnostic purposes, for example, to determine what ranges of primary

energy and what regions of phase space in particle production are important for various classes of events. Often, for such diagnostic purposes an approximate representation is adequate.

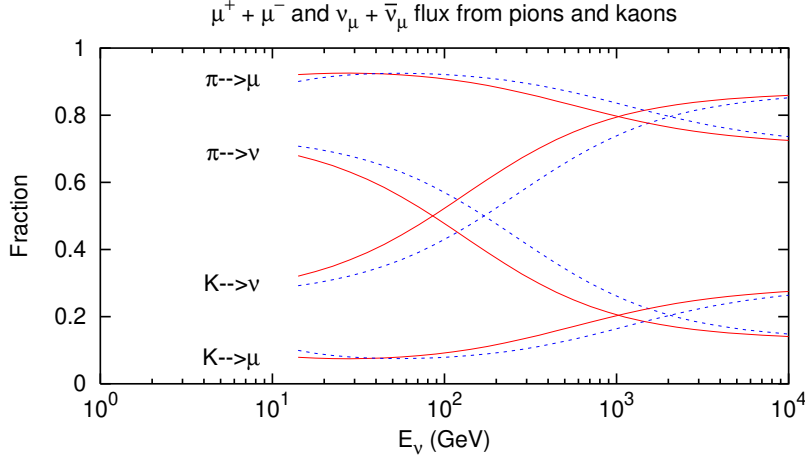


Figure 4: Fractional contribution of pions and kaons to the flux of muons and neutrinos. For pions the bottom curve of each pair is for the vertical and the top curve for zenith angle of 60° . The reverse is true for the kaon fractions.

The analytic approximations apply at high energy ($E_\nu \gg 1$ GeV) and hold for a power-law primary spectrum and inclusive cross sections that obey Feynman scaling in the fragmentation region. With these assumptions, the differential flux of $\nu_\mu + \bar{\nu}_\mu$ from decay of pions and kaons is

$$\frac{dN_\nu}{dE_\nu} = \frac{\phi_N(E_\nu)}{(1 - Z_{NN})(\gamma + 1)} \left\{ \left[\frac{Z_{N\pi}(1 - r_\pi)^\gamma}{1 + B_{\pi\nu} \cos \theta E_\nu / \epsilon_\pi} \right] + 0.635 \left[\frac{Z_{NK}(1 - r_K)^\gamma}{1 + B_{K\nu} \cos \theta E_\nu / \epsilon_K} \right] \right\}, \quad (6)$$

where

$$\phi(E_0) = \frac{dN}{dE_0} = A \times E_0^{-(\gamma+1)} \quad (7)$$

is the differential primary spectrum of nucleons of energy E_0 . The neutrino flux in Eq. 6 is proportional to the primary spectrum evaluated at the energy of the neutrino. The constants $r_i = m_\mu^2/m_i^2$ for $i = (\pi, K)$, and the constants

B_i depend hadron attenuation lengths as well as decay kinematics (41). The expression for the flux of $\mu^+ + \mu^-$ has the same form but with different kinematical factors. Similar (somewhat more complex) formulas also exist for neutrinos from decay of muons (42). The approximations become increasingly accurate as energy increases. Eq. 6 displays the features of angular dependence and the relative importance of kaons as described above and illustrated in Fig. 4.

Table 1: Parameters for atmospheric $\nu_\mu + \bar{\nu}_\mu$ from π, K -decay

Mass-square ratios	r_π	r_K	B_π	B_K
& B-factors:	0.573	.046	2.77	1.18
Characteristic E_{decay} :	ϵ_π	ϵ_K	ϵ_{charm}	
	115 GeV	850 GeV	$\sim 5 \times 10^7$ GeV	
Z-factors:	Z_N	Z_π	Z_K	
	0.30	0.079	0.0118	

The physics of production of the parent pions and kaons is contained in the spectrum-weighted moments,

$$Z_{N \rightarrow \pi(K)} = \int_0^1 dx (x)^{\gamma-1} F_{N \rightarrow \pi(K)}(x), \text{ etc.}, \quad (8)$$

where

$$F_{N\pi}(E_\pi, E_N) = \frac{E_\pi}{\sigma_N} \frac{d\sigma(E_\pi, E_N)}{dE_\pi} \quad (9)$$

is the normalized inclusive cross section for $N + \text{air} \rightarrow \pi^\pm + X$. The integrand of the spectrum-weighted moment in Eq. 8 displays the regions of longitudinal phase space in nucleon interactions that are most important for production of neutrinos (43).

Table 1 shows a sample set of parameters for the analytic formulas. The same formalism can be used to include neutrinos from decay of charmed particles.

These eventually dominate the spectrum at sufficiently high energy because of their short decay length (and correspondingly large critical energy).

2.3 Response functions

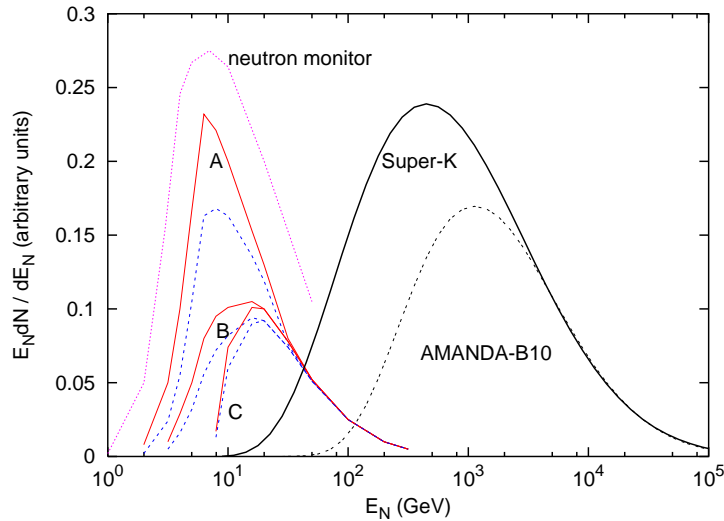


Figure 5: Response to primary energy for several classes of interactions of $\nu_\mu + \bar{\nu}_\mu$: sub-GeV events (A: no cutoff; B: events from the lower hemisphere; C: events from upper hemisphere at Super-K); vertically upward, throughgoing muons at Super-K and neutrino-induced muons in AMANDA-B10. For the sub-GeV events, each pair of curves shows the range of the signal between minimum (solid) and maximum (dashed) level of solar activity. The dotted curve shows a typical response function for a neutron monitor, to be discussed in §3.3. (The neutron monitor response is plotted *vs* rigidity rather than energy.)

Response functions give the distributions of primary energy/nucleon that produce neutrinos of a given energy (or distribution of energies). Since the uncertainty in the primary spectrum depends on energy, these functions can be used to evaluate the contribution of this source of uncertainty to the calculated neutrino

flux.

For the sub-GeV events the neutrino energies are low enough so that geomagnetic cutoffs and solar modulation become important. These points are illustrated by the curves labelled A, B and C in Fig. 5 and will be discussed further below. Fig. 5 also shows the response for vertically upward throughgoing muons at Super-K and for upward muons in AMANDA B10 as estimated with the approximations of Ref. (43). The threshold for the neutrino-induced upward muon at Super-K is ≈ 7 GeV (vertical) and about an order of magnitude higher for AMANDA B10 (26).

3 Primary Spectrum

Here we describe the primary spectrum inside the heliosphere as it would be measured without the influence of the geomagnetic field. It is important to note that, except for geomagnetic effects, the primary cosmic-ray flux is nearly isotropic. Compton and Getting (44) pointed out that the motion of the earth due to galactic rotation at ~ 300 km/s would lead to an asymmetry of order 1% in the relativistic cosmic rays if their sources were external to the galaxy. Any asymmetry due to the motion of the earth relative to the cosmic-ray gas has come to be known as the Compton-Getting effect. It is now believed that most cosmic rays originate inside the galaxy, so one might expect a smaller anisotropy due to the peculiar motion of the solar system at ~ 20 km/s relative to the galactic rotation. Sidereal cosmic-ray anisotropies have been measured to be at the level of $< 0.1\%$ (45), although a recent analysis (46) indicates a more complex origin than the Compton-Getting effect. In any case, such asymmetries are too small to affect the neutrino flux significantly. We discuss the geomagnetic effects,

which are important for sub-GeV neutrinos, in the next section.

3.1 Summary of data on protons and helium

In the last decade a series of measurements with superconducting magnetic spectrometers has greatly improved our knowledge of primary cosmic-ray spectra up to 100 GeV/nucleon. At higher energies the situation is not as good. Fig. 6 is a summary of the data for protons and helium. The measurements below 100 GeV are made with balloon-borne magnetic spectrometers (47, 48, 49, 50, 51, 52, 53) and by the AMS Space Shuttle flight (54). Measurements at higher energy have been made by balloon-borne calorimeters of various kinds (55, 56, 57, 58, 59). These do not capture all the energy of the primary, and as a consequence, the energy determination is not as precise as with a spectrometer.

Starting with the LEAP experiment (48), the measured fluxes have been consistently lower than that of Ref. (47), which had previously been the standard. Particularly remarkable is the close agreement between the BESS (53) and AMS (54) measurements of the proton flux. They agree with each other to better than 5% over their whole energy range. In contrast there is a systematic difference of about 15% between the BESS and AMS measurements of helium. Note, however, that only some 25 % of all nucleons is carried by helium and heavier nuclei, so such a difference corresponds to an uncertainty of ~ 3 % in the flux of nucleons.

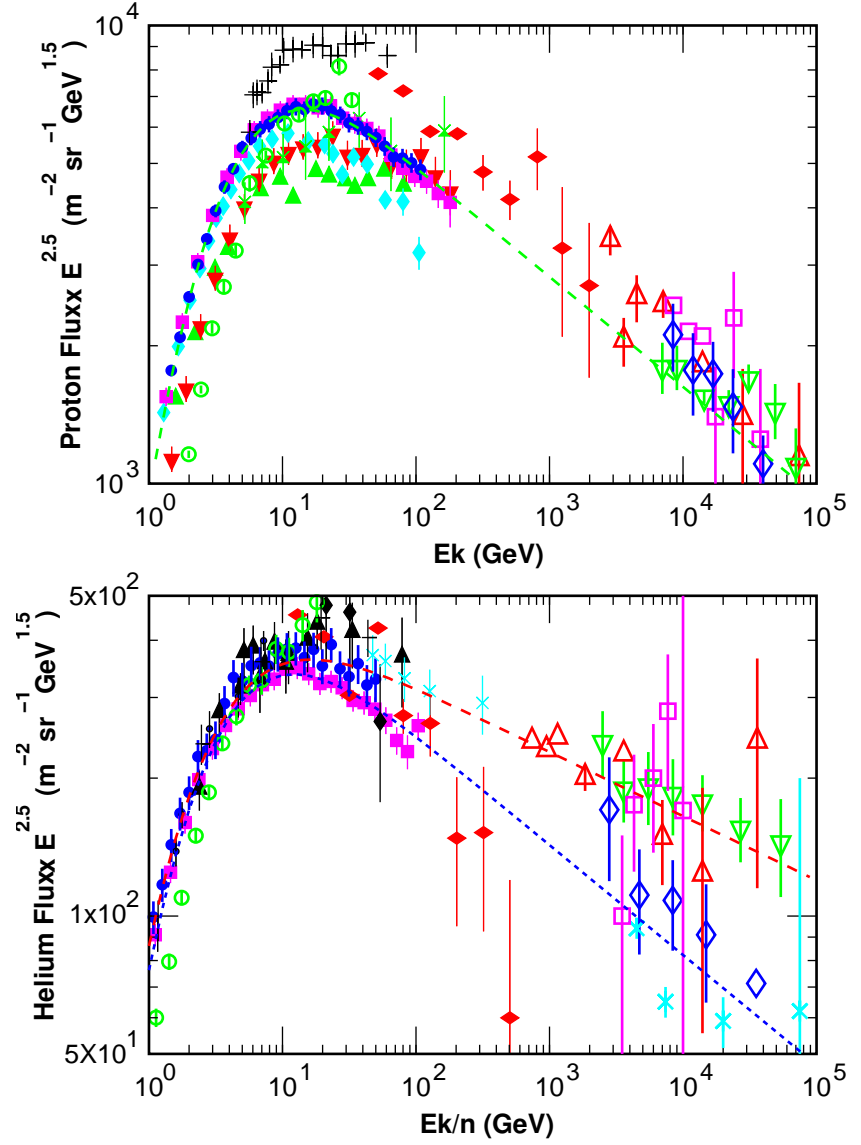


Figure 6: Observed flux of cosmic-ray protons and helium. The dashed lines show the fits described in the text. The data are: Webber (47)-crosses; LEAP (48)-upward triangles; MASS1 (49)-open circles; CAPRICE (51)-vertical diamonds; IMAX (52)-downward triangles; BESS98 (53)-circles; AMS (54)-squares; Ryan (55)-horizontal diamonds; JACEE (56)-downward open triangles; Ivanenko (57)-upward open triangles; Kawamura (59)-open squares; Runjob (58)-open diamonds.

Ref. (60) discusses the measurements of the primary spectrum in the context of atmospheric neutrinos. Fits of the form

$$\phi(E_k) = K \times \left(E_k + b \exp \left[-c\sqrt{E_k} \right] \right)^{-\alpha} \quad (10)$$

are given, with parameters as tabulated in Table 2. The fits for protons and helium are determined largely by the AMS (54) and BESS (53) data, with their small statistical uncertainties. They are shown as dashed lines in Fig. 6. Parameters for the three groups of heavy nuclei in Table 2 have been updated by Stanev (61) since publication of Ref. (60).

Table 2: Parameters for all five components in the fit of Eq. 10.

parameter/component	α	K	b	c
Hydrogen (A=1)	2.74±0.01	14900±600	2.15	0.21
He (A=4, high)	2.64±0.01	600±30	1.25	0.14
He (A=4, low)	2.74±0.03	750±100	1.50	0.30
CNO (A=14)	2.60±0.07	33.2±5	0.97	0.01
Mg-Si (A=25)	2.79±0.08	34.2±6	2.14	0.01
Iron (A=56)	2.68±0.01	4.45±0.50	3.07	0.41

3.2 Heavier nuclei and the all-nucleon spectrum

Production of pions and kaons in the atmosphere, and hence, the neutrino flux, depends essentially on the spectrum of nucleons as a function of energy-per-nucleon. Protons and neutrons must be treated separately to obtain the charge ratio and the correct $\bar{\nu}/\nu$ ratios. Bound and free protons must be passed separately through the geomagnetic filter since the relation between energy per nucleon and rigidity is different for free protons and for nuclei.

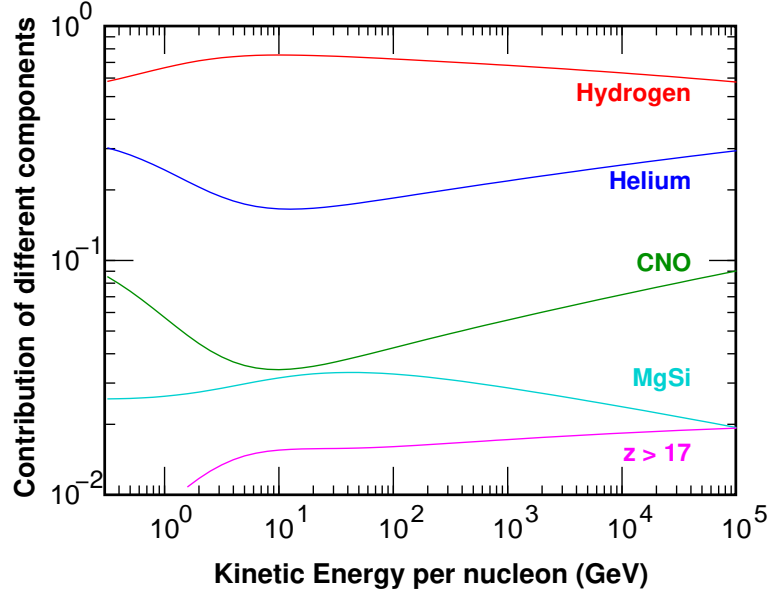


Figure 7: Fractional contributions of various nuclei to the all-nucleon spectrum (60).

A fit for the all-nucleon spectrum outside the magnetosphere corresponding to Eq. 10 can be constructed directly from Table 2. Fig. 7 shows the fractional contributions of protons, helium and three groups of heavy nuclei. In the energy range important for the contained neutrino interactions, protons contribute 75%, helium 15% and all heavier nuclei about 10%.

3.3 Solar modulation

The sun emits a magnetized plasma with a velocity of ≈ 400 km/s in the solar equatorial region and about twice as high over the solar poles (62). To reach the earth and interact in the atmosphere, galactic cosmic rays have to diffuse into the inner heliosphere against the outward flow of the turbulent solar wind, a process known as solar modulation. Particles of very low energy outside the heliosphere are nearly completely excluded, while higher energy particles lose energy as they

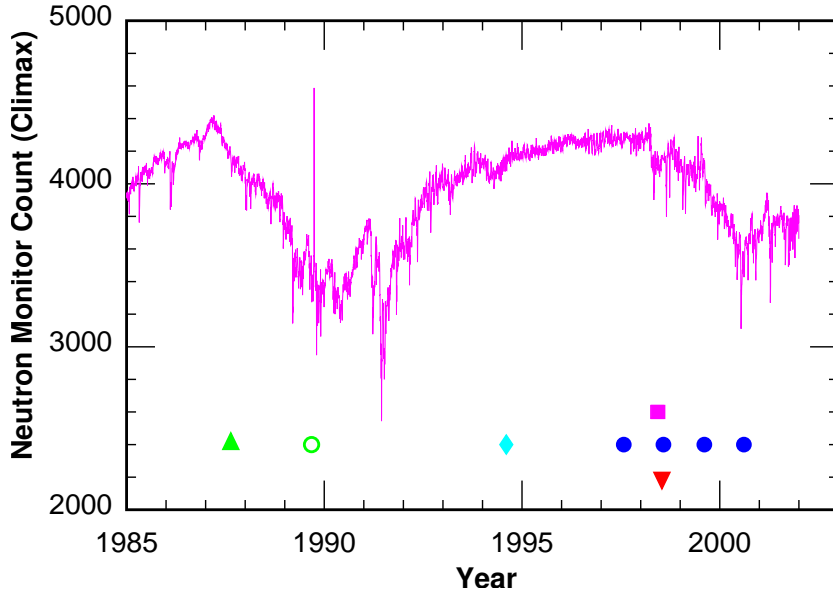


Figure 8: Record of count rates for the Climax neutron monitor (66). Times of the various flights are marked using the same symbols as in Fig. 6.

diffuse in. During periods of high solar activity (“solar maximum”) the turbulence in the solar wind is higher than during solar minimum and the low-energy portion of the spectrum is more suppressed.

A classic tool for study of solar modulation is the neutron monitor (63). Response functions for neutron monitors (64) are similar to the response for sub-GeV neutrinos, as illustrated by the dotted curve in Fig. 5. As a consequence, neutron monitor records (65, 66) provide an ideal tool for interpolating between the spectra measured at particular instants of the solar cycle. Fig. 8 is a plot of the Climax neutron monitor (66) with the dates of the flights on which the low-energy data in Fig. 6 were obtained. Except for MASS1 (49), most of the flights were close to solar minimum conditions, and the shapes of their low-energy spectra are similar. The MASS1 data, which were obtained in 1989 during solar maximum conditions, show extra suppression at low energy.

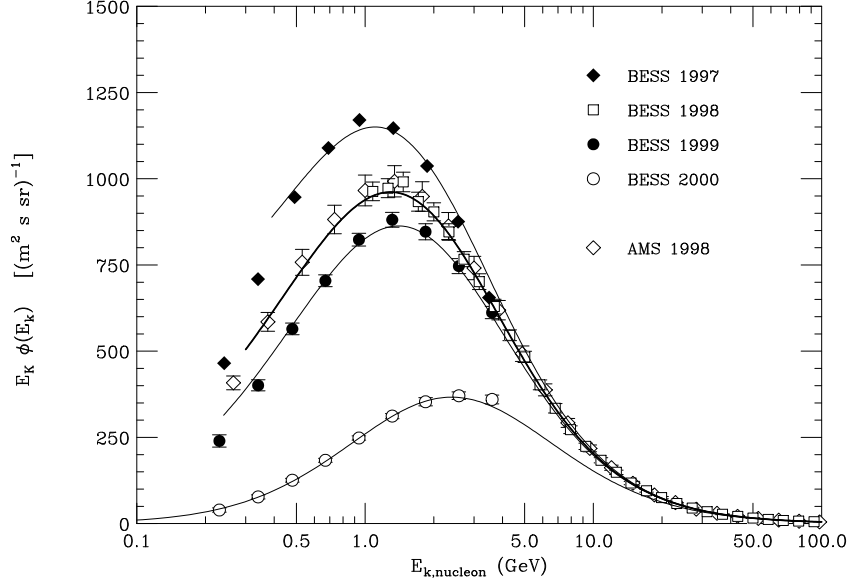


Figure 9: Proton spectra measured by BESS in 1997, 1998, 1999 and 2000 (70). Curves are explained in the text.

It is possible to use the neutron monitor count rate (N_m) as a parameter to relate the spectrum at one phase of the solar cycle to that at another. The parameterization of Ref. (67) was used in Ref. (35) to provide a multiplicative factor by which a time-independent reference spectrum is multiplied. The factor is a function both of particle momentum and N_m . Recently a new set of data taken with the BESS detector at three different levels of solar activity (including one in 2000 during solar maximum) has been published (70). We show these data, together with the BESS98 data from Fig. 6, in Fig. 9. The curves in Fig. 9 are obtained by Lipari (68) starting with Eq. 10 for the 1998 BESS data and using the force-field approximation (69). In this simple approximation the phase space density of particles is shifted down in energy by an amount $\Delta\Phi$ that depends only on N_m and not on momentum. When the BESS-2000 data for $E > 4$ GeV

becomes available it will be possible to refine the way the spectrum modulates as a function of energy. At the same time, the data should provide the basis for an improved understanding of solar modulation. In the meantime, we can estimate roughly (see Fig. 5) that solar modulation should be a 10% effect at Kamioka and a 20% effect at the high latitude sites, Soudan and Sudbury.

4 Geomagnetic effects

The geomagnetic field affects cosmic rays both outside and inside the atmosphere. Outside it acts as a filter which allows in particles of sufficiently high energy and excludes those of lower energy. Inside it bends charged secondaries causing some important effects which we discuss later. Whether a particle is allowed or forbidden is determined by its position, direction, and radius of curvature. Only those particles that interact in the atmosphere before curving back into space can contribute to the flux of atmospheric neutrinos. Because the effect depends on the gyroradius of a particle, the relevant kinematic variable is total momentum divided by total charge, i.e. rigidity.

In case of a dipole magnetic field centered on the earth, the cutoff rigidity can be expressed in an analytic form by Störmer's formula (71, 72):

$$R_S^\pm(r, \lambda_M, \theta, \varphi) = \left(\frac{M}{r^2} \right) \left\{ \frac{\cos^4 \lambda_M}{[1 + (1_\mp \cos^3 \lambda_M \sin \theta \sin \varphi)^{1/2}]^2} \right\}, \quad (11)$$

where r is the distance from the center of the earth and λ_M is the geomagnetic latitude, θ and φ define the arrival direction of the cosmic ray, and $M = 8.1 \times 10^{25} \text{ G cm}^3$ is the magnetic dipole moment of the earth. The azimuthal angle of the direction vector of the particle is φ , measured counterclockwise from magnetic north. Thus a particle arriving from the west has $\sin \varphi < 0$ giving a lower cutoff for a positive particle (upper sign in Eq. 11). A positive particle arriving from the

east has a higher cutoff. The scale is set by the maximum cutoff $eM/r_{\oplus}^2 = 60 \text{ GeV}$, which is the energy at which a proton approaching from the east at the equator will orbit the earth.

4.1 *Cutoffs for realistic magnetic field*

The actual magnetic field is more complicated than a symmetric dipole, and such a simple expression as Eq. 11 is not available. The geomagnetic field is generally expressed as a multipole expansion, and its global structure is well known (73).

The cutoff rigidity for a realistic geomagnetic field can be calculated by the back tracing technique. An anti-proton, which has the same mass as a proton but the opposite charge, is used as the test particle. We note that the change $e \leftrightarrow -e$ is equivalent to the change of $t \leftrightarrow -t$ in the equation of motion of a charged particle in a magnetic field. We launch anti-protons from the top of the atmosphere of the Earth, varying the position and direction to obtain the coverage needed for a given detector location. Standard practice is to define the escape sphere at 10 earth radii. The rigidity cutoff is calculated as the minimum momentum with which the test particle escapes from the geomagnetic field. For some directions at some locations the situation is still more complicated. There can in some cases also be forbidden trajectories in a narrow region just above the minimum cutoff (74).

The back tracing technique only tells us if there is a path along which a cosmic ray of a particular momentum and charge can reach the top of the atmosphere. To know the spectrum at the top of the atmosphere, however, one also needs Liouville's theorem, which ensures the conservation of particles in phase space. Then, assuming that the distribution of cosmic rays outside the heliosphere is

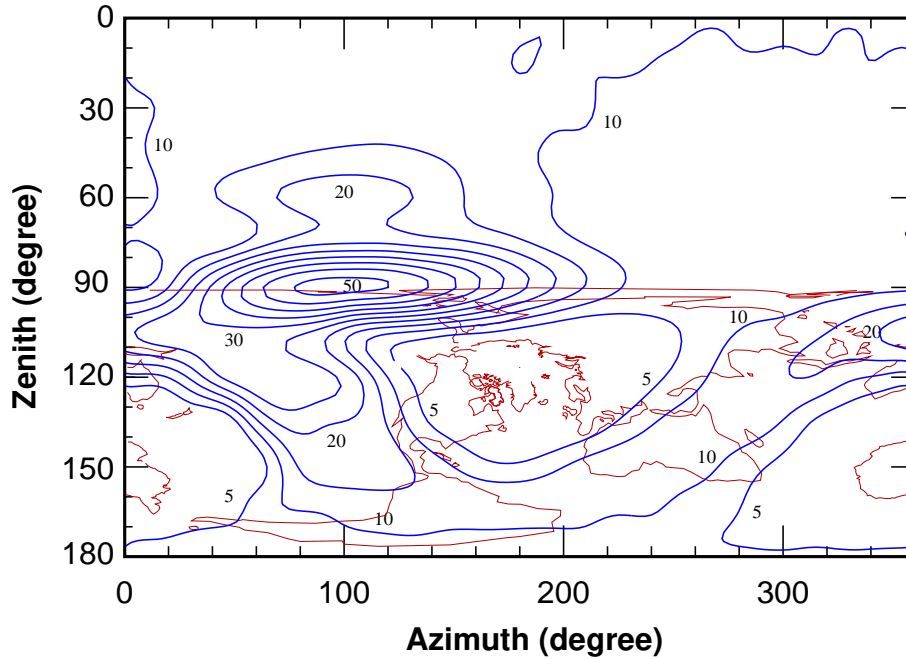


Figure 10: Contour map of the rigidity cutoff as seen from the Kamioka site, Rigidity cutoffs are shown as a function of arrival direction of the neutrino. (Zenith angle $> 90^\circ$ is for upward-moving particles.) An outline map of the continents is superimposed on the lower hemisphere.

isotropic and assuming no change in magnitude of momentum along the path, the flux of particles at the atmosphere has the same value as in interstellar space for allowed values of momentum.

For a one-dimensional calculation, one can make a contour map of the cutoffs for each detector as a function of direction along the line of sight from the detector. Each entry is the cutoff in the atmosphere where the neutrino trajectory originates. Such a contour map for the cutoffs at Kamioka is shown in Fig. 10 (35). In the case of a three dimensional calculation, the treatment of geomagnetic cutoffs is very considerably more complex. Since the direction of the neutrino can be at an angle relative to the primary cosmic ray that produced

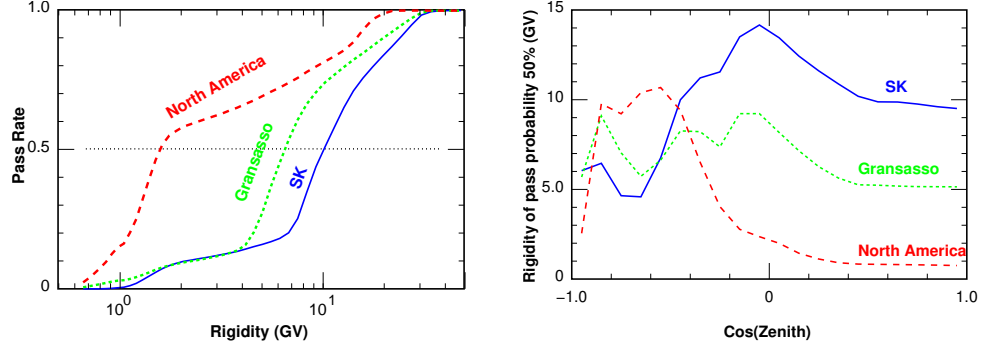


Figure 11: Cutoffs at three locations: north-central North America (Soudan, Sudbury); Gran Sasso; Kamioka. The left panel shows the passing rate as a function of rigidity integrated over all directions. The right panel shows the rigidity above which half the particles in the azimuthal band at each zenith angle reach the atmosphere. (Positive $\cos \theta$ refers to downward-moving particles.)

it, one needs the cutoffs for all directions at every point around the globe.

The qualitative effects of the geomagnetic cutoffs at different locations on the globe can be displayed by comparing averaged cutoffs. The left panel of Fig. 11 plots the fraction of 4π sr allowed as a function of rigidity. The second panel shows the cutoffs averaged over azimuth plotted as a function of zenith angle. (The average cutoff for a given zenith is defined as the rigidity at which 50% of the directions in the azimuth band are allowed.) The three locations are North America (Sudbury and Soudan), Gran Sasso and Kamioka in increasing order of average cutoff. While the average cutoffs for the lower hemisphere ($\cos \theta < -0.5$) are similar for all locations (because they involve averaging over large portions of the surface of the earth) the local cutoffs are quite different. In particular, the up-down ratio at Super-K is opposite to that at the high-latitude sites in North America. Moreover, the geomagnetic up-down ratio at Super-K is such as to suppress downward events, which is opposite to the observed pathlength

dependence.

4.2 East-West Effect

Kamioka is at a rather low geomagnetic latitude and has therefore a rather high local cutoff, ≈ 11 GV. In addition, there is a strong azimuthal asymmetry, with the cutoff higher for particles arriving from the east than from the west. The east-west asymmetry follows from the fact that the primary cosmic rays are positively charged. Historically, it was the east-west asymmetry that led to the conclusion that the primary cosmic rays are positively charged (75, 76). A remarkable feature of the Super-K is that it has been possible to measure (77) the classic east-west asymmetry of the primary cosmic rays as reflected in neutrinos (78, 35). Quantitative understanding of this feature of the data confirms that deviations of the atmospheric neutrino beam from isotropy can be understood entirely as arising from effects of the geomagnetic field.

In the Fig. 12, we show the experimental data with the predictions. It is seen that the experimental data agree with the predictions well within the experimental errors. However, Lipari pointed out that the azimuthal variation of ν_e events is somewhat larger than the predictions of the one-dimensional calculations, while the azimuthal variation of the ν_μ events is smaller (87). He argues that these details are a consequence of bending of muons by the geomagnetic field inside the atmosphere, which is neglected in the one-dimensional calculations.

Roughly speaking, the μ^+ bending enhances the E-W effect for the primary cosmic rays, since the μ^+ has the same charge as primary cosmic rays. On the other hand the μ^- bending works to cancel the E-W effects. Therefore the azimuthal variation of ν_e and $\bar{\nu}_\mu$ is enhanced by the muon bending above the

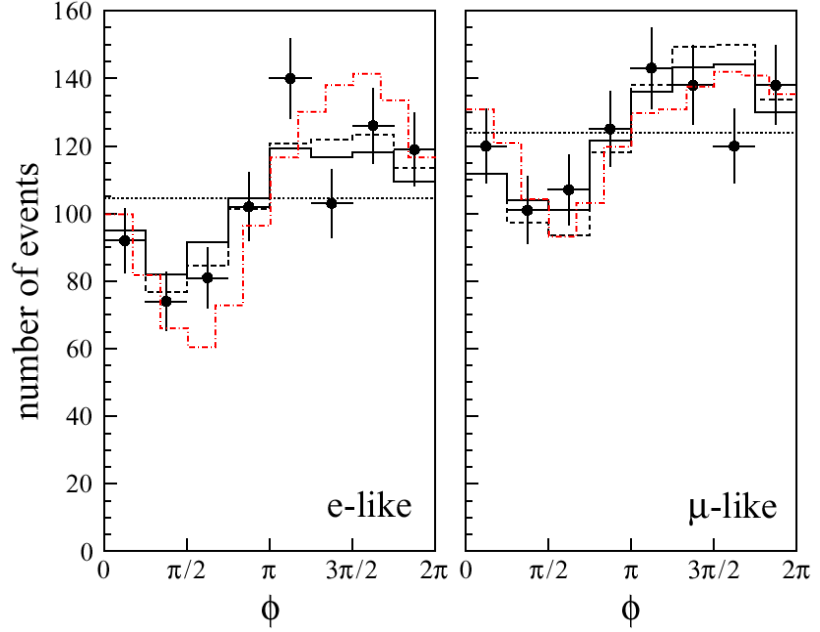


Figure 12: East West effect observed by neutrino. Data points are from SK experiment, and solid and dashed lines are prediction by using the one-dimensional calculation of Honda et al. and Bartol group. Dash-dot are predictions by Lipari taking into account the muon bending normalized by the average value.

prediction of the one-dimensional calculations. On the other hand, the azimuthal variation of $\bar{\nu}_e$ and ν_μ are reduced. Considering the fact that the interaction cross sections for ν 's are ~ 3 times larger than $\bar{\nu}$'s at ~ 1 GeV, the muon bending enhances the variation of electron events in the detector and reduces the variation of muon events.

In Fig. 12 the data are plotted as a function of azimuth for a fixed band of zenith angles. Thus any pathlength-dependence affects all events in the band in the same way. The fact that the observed azimuthal variation can be understood entirely as a consequence of geomagnetic effects therefore confirms that the observed pathlength dependence (i.e. dependence on zenith angle) is not due to a poorly understood geomagnetic effect, but is a consequence of pathlength-dependence

of the neutrinos.

4.3 Second (subcutoff) spectrum

The AMS detector on the Space Shuttle found and measured (80) at 380 km altitude a population of partially trapped particles below the local geomagnetic cutoff. This population is related to the cosmic-ray albedo previously known from stratospheric balloon flights above 30 kilometers (see, for example, (81, 82)). It originates when higher energy cosmic rays above the local geomagnetic cutoff interact in the atmosphere and produce secondaries that curve away from the earth. Some of the secondaries may be below the local geomagnetic cutoff, in which case they eventually re-enter the atmosphere as re-entrant albedo (83).

Several authors (84, 85, 86) have analyzed this “second spectrum” recently by performing 3-dimensional calculations which reproduce the data and allow them to make conclusions about its origin and properties. Since only a small fraction of the secondary nucleons move away from Earth, the intensity of the sub-cutoff population is significantly lower than would be the case in the absence of a geomagnetic field. In addition, a fraction of the particles in the equatorial region remains trapped for several cycles, so that the rate at which these particles re-enter the atmosphere is lower (by a factor equal to the inverse of the number of trapped cycles) than what is measured at 380 km. The reduction of the re-entrant flux is greatest in the equatorial region where the cutoff is generally high. On average, the re-entrant sub-cutoff flux above the threshold for significant pion production is always at least an order of magnitude below the flux at the cutoff energy (86). All these points are nicely illustrated in the figure from Ref. (86) that compares AMS data (80) with their calculations. The panels in Fig. 13

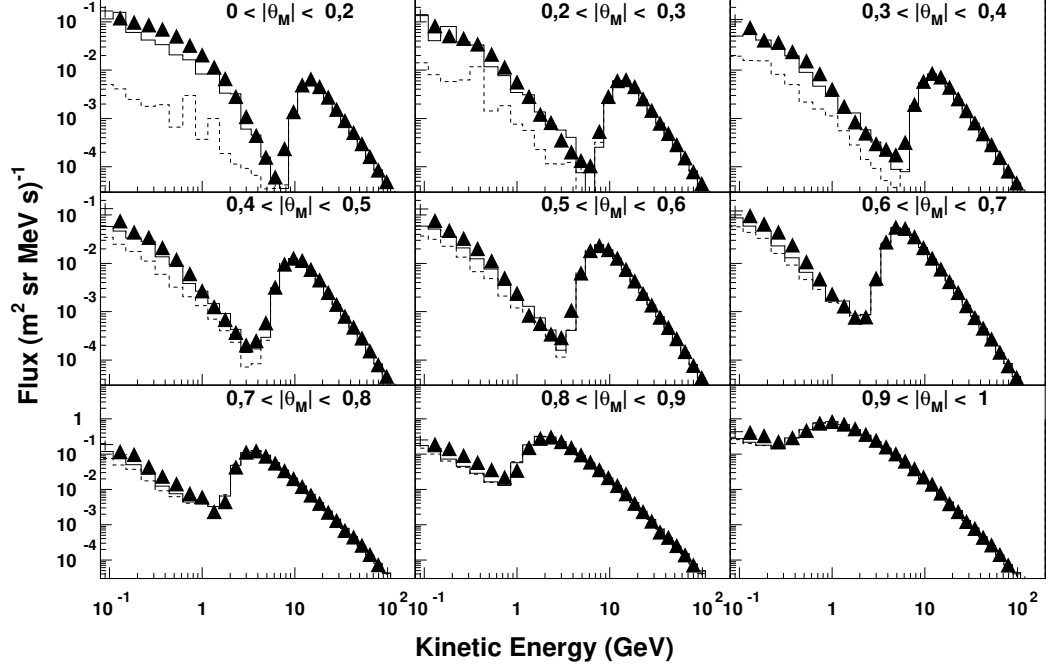


Figure 13: Proton spectrum measured (80) at various geomagnetic latitudes by the AMS detector on Space Shuttle compared to calculations of Ref. (86). The figure is from Ref. (86).

show a succession of bins of geomagnetic latitude from the equator ($\Theta_M = 0$) to the poles ($\Theta_M = \pm 1$). The dashed line shows the reduced rate at which the sub-cutoff particles re-enter the atmosphere and so become available for neutrino production. In addition, the neutrino yield per incident particle is lower below the cutoff than above. As a consequence, the contribution of the sub-cutoff particles to the neutrino flux is small, though it remains to be calculated precisely.

It is interesting to note that the contribution of the subcutoff particles to the neutrino flux is included in the one-dimensional calculation since all secondary nucleons are assumed to go forward.

5 Hadronic interactions

The third factor in Eq. 3 is the yield of neutrinos per incident cosmic-ray nucleon. For fixed E_ν , the yields grow strongly with increasing primary energy. At the same time, the primary spectrum falls quickly as energy increases, to give distributions like those shown in Fig. 5.

Yields are calculated for events generated from primary cosmic rays of various energies and mass, and the events are then weighted according to an appropriate energy spectrum and mass composition. Several technical details of the cascade calculations, in particular muon energy loss and decay, require care in their implementation. The only fundamental source of uncertainty in the yields, however, is from the treatment of particle production in the individual collisions that make up the atmospheric cascades.

Two independent flux calculations (32, 35) have been widely used for interpretation of measurements of atmospheric neutrinos. Both are one-dimensional. More recently, new, three-dimensional calculations have been made (34, 79, 36), which remove the major technical approximation of the original calculations. Differences among the calculations are at the level of 20% in overall magnitude and 5% or less in the ratios ν_e/ν_μ and $\bar{\nu}/\nu$. Although there are significant differences between the 3D and 1D calculations (34, 79, 36), especially in the angular distributions of sub-GeV neutrinos near the horizon, the major differences are due rather to differences in the treatment of pion production and in the primary spectrum.

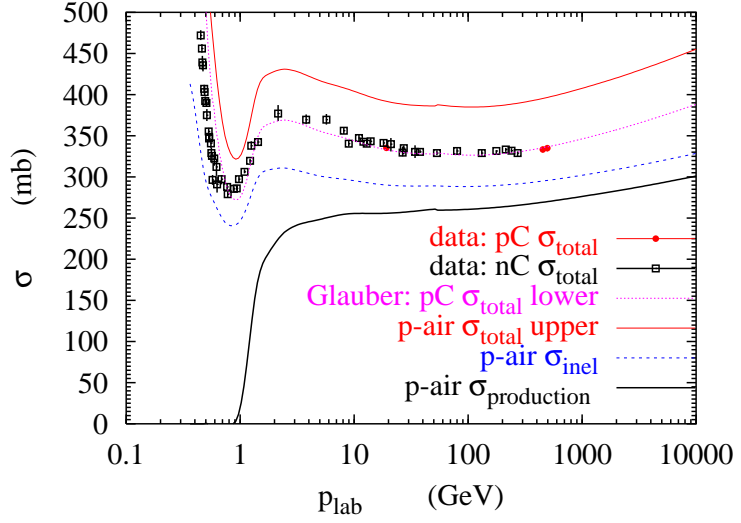


Figure 14: Plot of the total, inelastic and production p-air cross sections. Also shown is a comparison of the p-carbon total cross section with accelerator data. The step in the p-air production cross section at 1 GeV/c corresponds to the onset of significant pion production.

5.1 Cross sections

The starting point for calculation of the atmospheric cascade is a set of energy-dependent interaction lengths for the various particles in the cascade. In the approximation that the target in each interaction is treated as an average “air” nucleus, $\lambda_i(\text{g/cm}^2) \approx 14.5m_p/\sigma$. It is straightforward to treat the components separately with partial interaction lengths for 78% nitrogen, 21% oxygen and 1% argon by volume. If (as in Ref. (32)) quasi-elastic interactions in which the target nucleus fragments without pion production are not included when nucleons interact in the atmosphere, then the corresponding partial inelastic cross section in which at least one secondary meson is produced is used to obtain the interaction lengths. If quasi-elastic processes are included in the event generator (as in Ref. (100)) then the total inelastic cross sections are used to obtain the

interaction lengths. Fig. 14 shows a plot of the nucleon-air cross sections (σ_{tot} , σ_{prod} and σ_{inel}). The quasi-elastic cross section is $\sigma_{QE} = \sigma_{inel} - \sigma_{prod}$.

The p-air cross sections have been calculated (89) from the parameters of the measured proton-proton cross section (elastic and total cross section, slope parameter and ratio of real to imaginary part of the forward scattering amplitude) using the Glauber multiple scattering formalism (90). To illustrate how well the formalism works, Fig. 14 also shows the total cross section for carbon calculated in the same way compared with an extensive collection of data (91). For lab energies corresponding to $\sqrt{s} > 2$ TeV, where there are not yet any direct measurements of the proton-proton cross sections, the proton-air cross section becomes somewhat uncertain. Since $\sqrt{s} = 2$ TeV is equivalent to a lab energy of ≈ 2 PeV, this is not an important source of uncertainty even for the neutrino-induced muons.

Concerning treatment of incident nuclei, there are two aspects to consider. First, one needs a set of cross sections and interaction lengths for the various nuclei. In addition, an algorithm for production of secondary particles is needed. The usual approach is to neglect possible coherent effects and use the Glauber multiple scattering theory to determine a number of nucleon-nucleon interactions in each encounter. This can be done with a monte carlo realization of the multiple scattering calculation to determine the number of interacting pairs event-by-event. Then the model for pion and kaon production in nucleon-nucleon collisions is invoked. A further approximation sometimes used is to determine the number of wounded nucleons in the projectile and then immediately use the model for particle production in nucleon-air collisions. In this approximation (92), incident nuclei of mass A and energy E are equivalent to A nucleons each of energy per nucleon E/A .

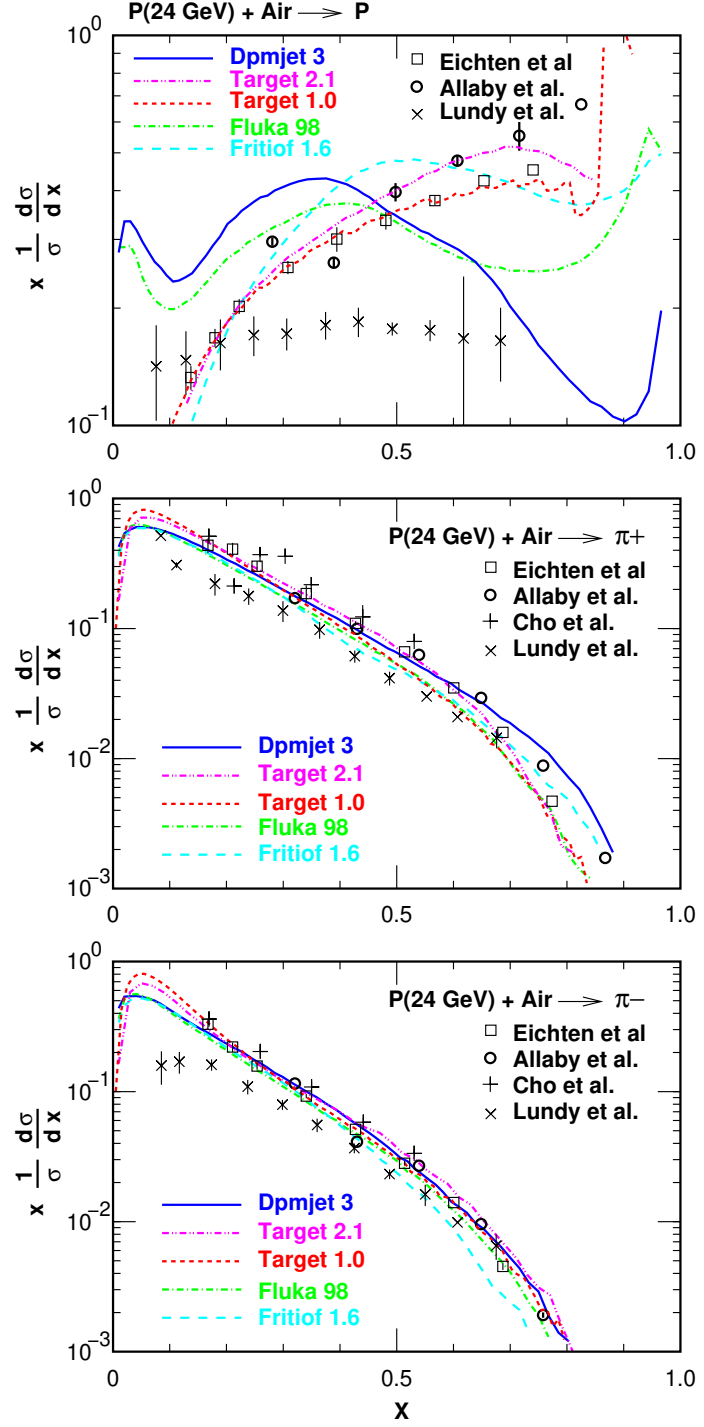


Figure 15: Inclusive cross sections for protons (top); π^+ and π^- (bottom).

5.2 Pion and kaon production by protons

The models of hadroproduction in use for calculations of the atmospheric neutrino flux are based in one way or another on accelerator data for protons on light nuclei. Most such experiments were done as studies for design of accelerator neutrino beams. A good example is the work of Cho *et al.* using 12.4 GeV/c beams at the Argonne ZGS on a beryllium target (93). They measured $d\sigma/dpd\Omega$ as a function of secondary particle momentum with the spectrometer at several angles. They then used a standard four-parameter fit to the double differential cross section (94) to find smooth fits to the data. Similar experiments in the region around 20 GeV/c were made at the CERN PS (95, 96) and at 15 GeV/c at BNL (97). Figs. 15 shows the data from these and other (98) experiments as inclusive distributions integrated over angle using the same parameterization (94) to interpolate and extrapolate into unmeasured regions of phase space. The integration requires an extrapolation into unmeasured regions of transverse phase space, which leads to uncertainties in addition to those associated with the measurements, as discussed in Ref. (99).

The coverage of phase space in the accelerator measurements is generally not matched ideally to the atmospheric neutrino problem. Fig. 16 shows the regions of phase space for proton-air interactions that contribute to the sub-GeV neutrino signal at Super-K, as calculated with the FLUKA program (100, 101). The important region shifts to the right for higher energy neutrinos in a way that can be estimated from the response functions discussed above (see Fig. 5). Superimposed on the figure are the regions of phase space covered by the main data sets used for tuning models of hadroproduction for calculation of atmospheric neutrinos. One can note in particular that the region for $p_{beam} \geq 20$ GeV/c and

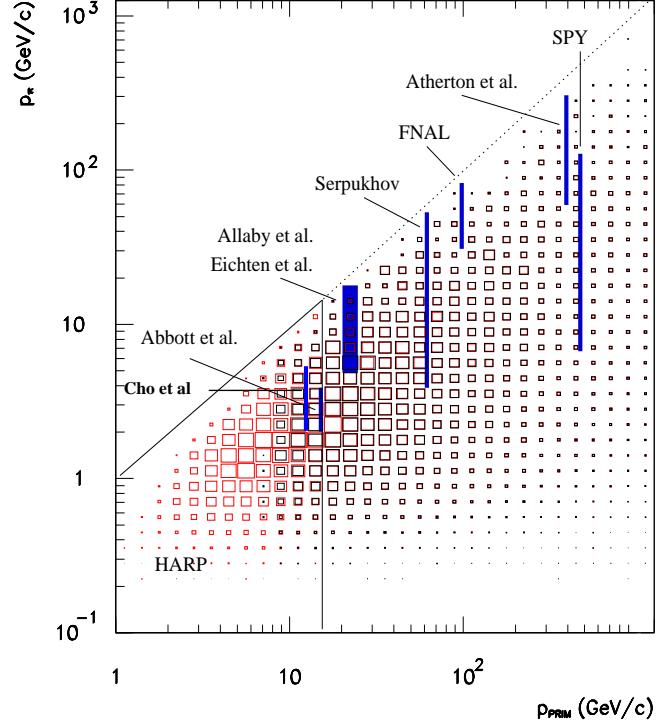


Figure 16: Weighted phase space distribution for sub-GeV atmospheric neutrinos.

$p_\pi < 4$ GeV that is important for the sub-GeV events is not covered.

The curves in Fig. 15 show some of the inclusive cross sections in use for calculations of atmospheric neutrinos. Dpmjet3 (102) is the event generator currently used by Honda et al. (36), who previously (35) used Fritiof 1.6 (103). Target 1.0 is the event generator of the Bartol group (32), and Target 2.1 is a preliminary revised version (33). The calculation of Battistoni et al. (34) uses the interaction model embedded in the FLUKA (100) cascade program.

The differences shown here are one of two main components responsible for the differences at the level of 15% among the calculations of Refs. (32, 35, 34) and (36, 33). The other main factor is the treatment of the primary spectrum. We comment further on these differences in the next section.

The process $p \rightarrow \Lambda K^+$ makes an important contribution to production of

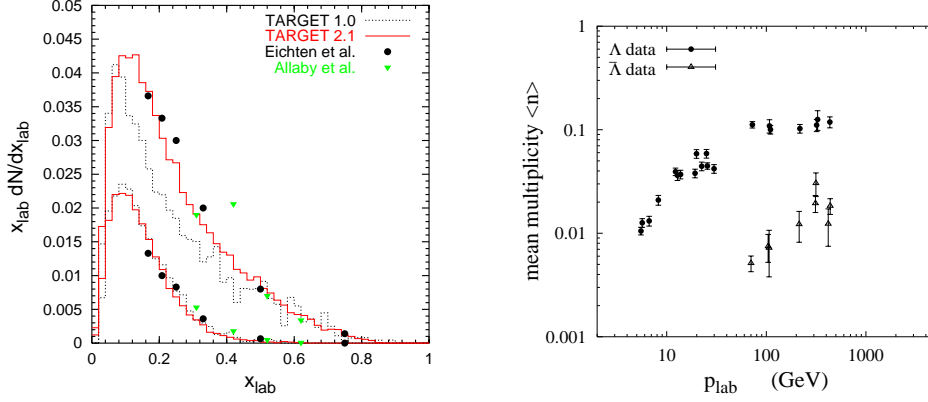


Figure 17: Left panel: Integrated inclusive cross sections for kaon production from Ref. (99). The upper set of points and histograms is for K^+ , while the lower is for K^- . Right panel: Multiplicity of Λ and $\bar{\Lambda}$ production in proton-proton interactions from Refs. (104)

strangeness, and it accounts for the large excess of K^+ over K^- in the fragmentation region. The effect is clearly visible in Fig. 17a, and it becomes increasingly important at high energy as kaons begin to dominate the neutrino flux (see Fig. 4.) Fig. 17b summarizes data on production of Λ and $\bar{\Lambda}$ in pp collisions. The difference ($\Lambda - \bar{\Lambda}$) corresponds to $p \rightarrow \Lambda K^+$. Because of the steep primary spectrum, this process is weighted heavily in the spectrum-weighted moments for kaons that enter into the calculated fluxes of neutrinos.

5.3 High energies

At sufficiently high energy the most important contribution to the neutrino flux will come from decay of charmed hadrons, the “prompt” flux, so called because of the short lifetimes of charmed particles. The critical energy for charm decay is $\sim 5 \times 10^7$ GeV. Thus the neutrinos from decay of charmed hadrons continue with the same spectral index as the primary cosmic-ray spectrum up to this energy,

while the neutrinos from decay of pions and kaons become steeper at much lower energy. Moreover, the prompt contribution is isotropic up to $\sim 10^7$ GeV while the contribution from pions and kaons is proportional to $\sec(\theta)$ for $E_\nu \gg 1$ TeV. As a consequence, even though $Z_{\text{charm}} \ll Z_{\pi,K}$, the contribution from charm decay dominates the neutrino spectrum at sufficiently high energy.

Predictions in the literature for the crossover energy differ by several orders of magnitude. Costa (105) surveys a wide range of calculations of prompt leptons. An analysis of the angular dependence of measurements of high-energy atmospheric muons (fitting to an isotropic plus a secant θ term) (106) suggests that the crossover energy may be as low as ~ 10 TeV. At the other extreme, in a perturbative QCD calculation, Thunman et al. (107) showed the crossover only around $E_\nu \sim 1000$ TeV. A more recent improved QCD calculation (108) puts the crossover around 100 TeV.

A concern with the perturbative QCD approach in the context of prompt cosmic-ray leptons is that it does not explicitly include the charm analog of $p \rightarrow \Lambda K^+$ discussed above. The Λ multiplicity plot in Fig. 17b allows an estimate of the probability per interaction of producing a forward ΛK^+ pair as ≈ 0.04 (by subtracting $\bar{\Lambda}$ from Λ and dividing by 2 to get the forward-moving particles). If we assume the production of massive hadrons with similar quark content is inversely proportional to the square of the masses (109), then we can estimate the probability of the corresponding charmed process $p \rightarrow \Lambda_C D^0$ as

$$P_{\text{forward charm}} \sim 0.04 \times \left(\frac{M_\Lambda + M_K}{M_{\Lambda_C} + M_D} \right)^2 \sim 0.006. \quad (12)$$

The actual calculation of the prompt lepton spectrum requires an assumption about the shapes of the inclusive cross section for production of the various charmed hadrons as well as accounting for the various relevant branching ra-

tios and decay distributions. Bugaev *et al.* (110) have systematically calculated prompt muon production in a recombination quark-parton model, which explicitly includes the important fragmentation process.

6 Comparison of neutrino flux calculations

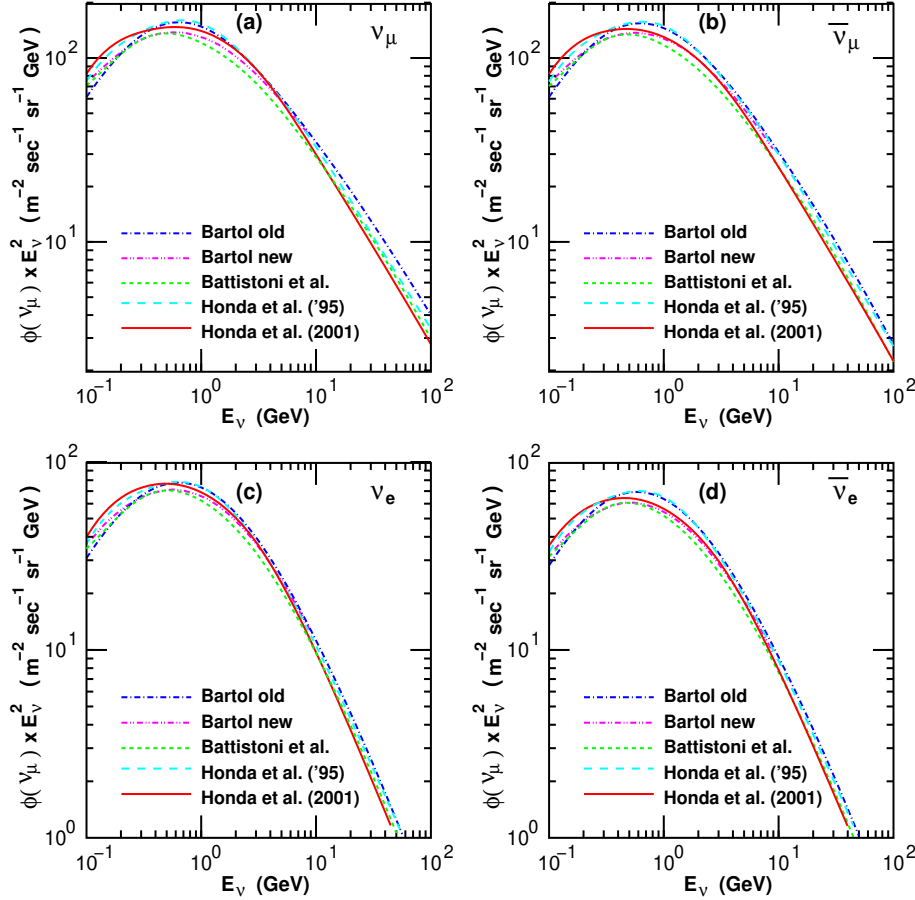


Figure 18: Comparison of neutrino flux calculations for the location of Kamioka averaged over all directions.

Comparing independent calculations is one way to assess the uncertainty in our knowledge of the atmospheric neutrino flux. Fig. 18 is a plot of the flux at Kamioka as calculated by three groups. The calculations of the Bartol group (32) and Honda *et al.* (35), both one-dimensional, are quite similar between 300 MeV

and 10 GeV, but the similarity results to some extent from compensating differences in input. The primary spectrum normalization is higher in Ref. (35) than in Ref. (32) while the pion production is lower. In contrast, the three-dimensional calculation of Battistoni *et al.* (34) uses exactly the same primary spectrum as Ref. (32) and finds a neutrino flux some 15% lower in the same energy region. As mentioned above, this difference is primarily a consequence of differences in pion production and not a consequence of the 3-dimensional nature of the calculation. The new one-dimensional calculation of Honda *et al.* uses a new model for pion production and a new and lower primary spectrum.

The interaction models used by these three groups represent three different approaches to the problem. Target is a simple phenomenological representation of pion and kaon production in interactions of protons, pions and kaons with light nuclei (33). Energy conservation is used as an important constraint in adjusting fits to the data. When events are generated, the fragment nucleon from the projectile is selected first, and the remaining energy distributed among pions. As a consequence, the fit to the fast nucleons is of primary importance. Honda *et al.* use more sophisticated event generators designed for monte carlo studies at accelerators, Fritiof 1.6 in Ref. (35) and Dpmjet3 more recently (36). FLUKA (100) is a cascade code that includes generation and propagation of secondary particles of all types in hadronic interactions of all types as an integral part of a cascade code adaptable for any purpose.

To focus on differences caused by the treatment of hadronic interactions, we refer to Fig. 19. Exactly the same primary spectrum and composition (that from Ref. (32)) have been used by Battistoni *et al.* (34) and by the Bartol group (32, 33). Although different primary spectra have been used in Refs. (35, 36), the

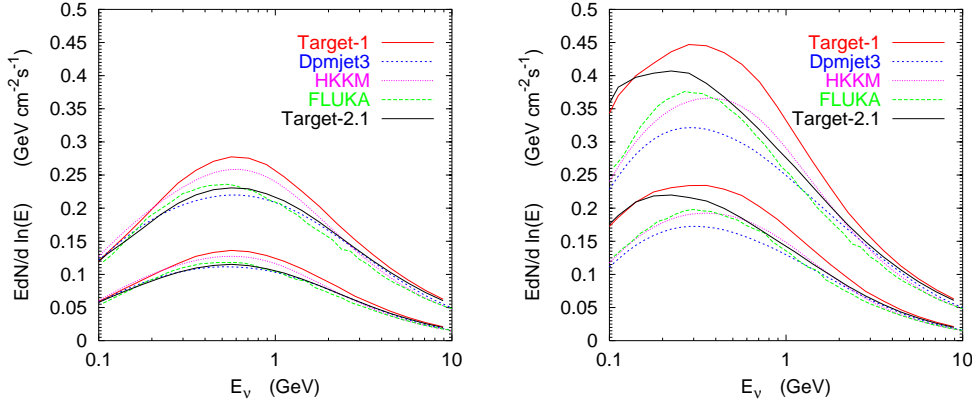


Figure 19: Angle-integrated neutrino fluxes ($\nu + \bar{\nu}/3$) at Kamioka (left) and Soudan (right) with several different interaction models: HKKM (35), Dpmjet3 (36), FLUKA (34), Target 1.0 (32) and Target 2.1 (33). The upper set of curves is for muon neutrinos and the lower set for electron neutrinos.

results shown here are from special calculations with the hadronic interaction models used in the published paper but using a primary spectrum identical to that of Ref. (32). Therefore, the only differences among these results are due to the differences in treatment of hadronic interactions. It should be possible to trace the differences in the neutrino fluxes shown here back to differences in interaction models such as those shown in Fig. 15. For example, the excess of pions in ~ 20 GeV interactions in Target 1.0 as compared to Target 2.1 and FLUKA corresponds to the larger calculated flux at Kamioka. The larger difference among the three calculations at Soudan points to differences in treatment of low-energy interactions that are important at Soudan but not at Kamioka with its higher cutoff.

In the past two years several new calculations of the flux of atmospheric neutrinos have appeared. They are summarized in Table 3 with a comment indicating their normalization relative to Ref. (34). Some of the recent calculations show

rather large differences from those discussed so far. The comparisons discussed above, however, suggest that uncertainties in normalization due to hadronic interactions are $< \pm 15\%$ (and somewhat larger at higher energy where the kaon contribution is more important). Differences in ratios such as ν_e/ν_μ are significantly smaller, at the level of 5% (see Fig. 3). Combining a $\pm 15\%$ estimate of uncertainty from hadronic interactions in quadrature with an estimate of $\pm 20\%$ for the primary spectrum gives an estimated uncertainty of $\pm 25\%$. Even if the estimates are simply added algebraically, it seems difficult to account for differences of a factor of two within the uncertainties in the input.

Table 3: Calculations of the atmospheric neutrino flux

Reference		Comment
FLUKA (34)	3D	1
New Bartol (33)	1D	≈ 1 (preliminary)
Honda <i>et al.</i> (36)	3D	+10 to 15%
SNO sub-group (111)	3D	~ 1
Fiorentini <i>et al.</i> (112)	1D	-20% for sub-GeV; ~ 1 for $> \text{GeV}$
CORSIKA (113)	3D	~ 1 (preliminary)
Grenoble (114)	3D	$\sim 1/2$
Plyaskin (115)	3D	$< 1/2$

7 Three-dimensional calculations

The major technical limitation of most calculations of the atmospheric neutrino flux until recently is that they are one-dimensional; in other words, it is assumed that all secondaries move in the direction of the primary particle from which

they descend. This approximation neglects the transverse momentum of the secondaries as well as their bending in the geomagnetic field as they propagate. The latter is most important for muons and their decay products because of the muon's long decay length. A muon with Lorentz factor γ typically bends by an angle

$$\theta \sim \gamma c \tau_\mu / r_L, \quad (13)$$

where $r_L \approx E_\mu / eB$ is its gyroradius in the geomagnetic field. Dependence on E_μ cancels in Eq. 13, and typical bending is $\sim 3^\circ$ for a muon in a field of order 0.3 Gauss. This is independent of energy for particles with trajectories such that their potential pathlength before reaching the ground exceeds their decay length. As a consequence, muon bending can be noticeable even in the multi-GeV range, as in the case of the modification of the East-West effect reviewed in §4.2.

The effect of transverse momentum, on the other hand, becomes increasingly important at low energy. Since the distribution of transverse momentum of secondaries in hadronic interactions is nearly independent of energy, with $\langle p_T \rangle \approx 300$ MeV for pions, the corresponding angular deviation is inversely proportional to energy, of order

$$\frac{p_T}{E_\pi} \sim \frac{0.1}{E_\nu(\text{GeV})} \quad (14)$$

in radians. The 3D effects are thus most important in the sub-GeV region.

Three-dimensional calculations of the neutrino flux present a significant technical challenge. A full 3D calculation without any approximations has to sample primary cosmic rays uniformly and isotropically in the downward half hemisphere at every point on the globe, taking account of the cutoff for every direction at each point. The created neutrinos will then also be nearly isotropic in the downward hemisphere (except for geomagnetic cutoff effects), and all but a small fraction

of order $A/R_{\oplus}^2 \sim 10^{-5}$ will be discarded. (Here A is the projected area of the detector and R_{\oplus} the radius of the earth.) On the other hand, in a one-dimensional calculation, only cosmic rays heading toward the detector are sampled, and all the neutrinos go through the detector. Thus, the one-dimensional calculation is a very efficient approximation.

Several approaches have been used to make the 3-dimensional calculation more tractable. Tserkovnyak et al. assumed a huge detector size(111); Battistoni et al. assumed spherical symmetry, ignoring the geomagnetic field inside the atmosphere(34); and Honda et al. assumed a dipole magnetic field and also a huge detector(88). In his 3D calculation (79) Lipari divided the Earth's surface into five detector zones. A preliminary version of a full 3D calculation without approximations uses a modified version of Corsika and the DPMjet interaction model (113).

7.1 *Geometry of neutrino production*

The most prominent feature of three-dimensional calculations is the neutrino flux enhancement near the horizon, as illustrated in Fig. 20 from Ref. (88). This enhancement is a geometrical effect not present in the one-dimensional calculations. Fig. 20 compares 3D and 1D calculations specifically at Kamioka, where the angular dependence results from a complex combination of the physics of neutrino production, geomagnetic effects and geometry. Before discussing the figure in detail, a digression on the geometry of neutrino production will be helpful.

Lipari (79) has given a detailed explanation of the origin of the excess of low energy neutrinos near the horizon in the 3D calculation, starting from an analysis in which all neutrinos are produced in a shell of constant altitude $h \sim 15$ km

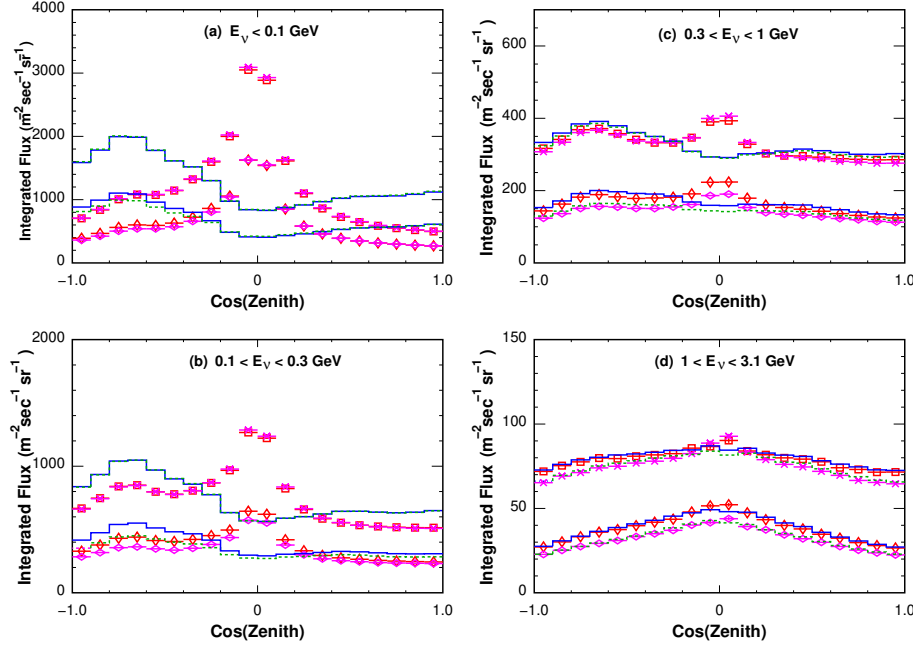


Figure 20: Comparison of three-dimensional and one-dimensional calculations of neutrino fluxes at Super-K (88). Squares are for ν_μ , asterisks for $\bar{\nu}_\mu$, vertical diamonds for ν_e , and horizontal diamonds for $\bar{\nu}_e$ for three dimensional calculation. The solid line histograms show the ν fluxes, and the dotted ones the $\bar{\nu}$ fluxes for the one dimensional calculation. The panels show four bins of neutrino energy: a) 0 – 0.1 GeV, b) 0.1 – 0.3 GeV, c) 0.3 – 1 GeV, and d) 1 – 3.1 GeV. The fluxes are averaged over all azimuthal angles in 20 bands of $\cos(\theta)$ from -1 (straight up) to $+1$ (vertically downward moving).

and geomagnetic effects are neglected. We follow his argument, generalizing it somewhat to display also the up-down symmetry of the neutrino flux that characterizes both the 3D and the 1D calculations in the absence of geomagnetic effects. Fig. 21 illustrates the detector A at a distance $r_A \approx R_\oplus$ from the center of the earth surrounded by a shell of radius $r_S \approx R_\oplus + h$ centered around the Earth. Eventually, an integral has to be made over the production altitudes (h) of the

neutrinos. Most neutrino production occurs in a band of altitude $10 < h < 20$ km, which is a thin shell compared to the radius of the Earth.

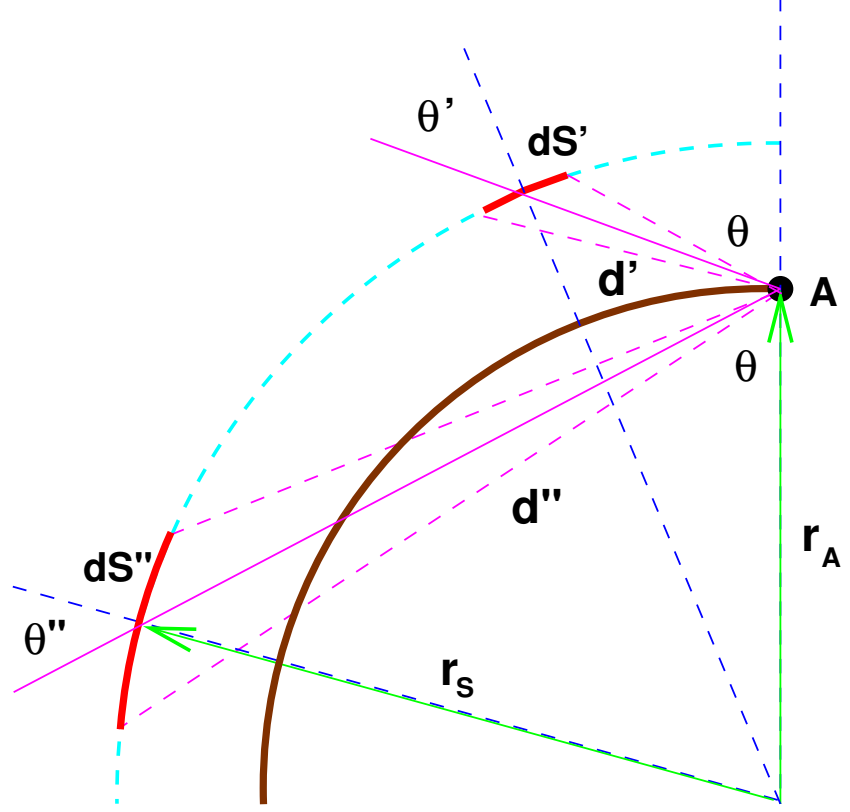


Figure 21: Geometry of atmospheric neutrino production (see text). The detector is at A, and we compare a neutrino entering from above the horizon at zenith angle θ with one entering from below the horizon at the same nadir angle. The angles $\theta' = \theta''$ are the apparent local zenith angles in the production regions, indicated by the heavily shaded arcs.

We consider neutrino emission from two patches of the production shell with area dS' and dS'' above and below the horizontal at the same zenith and nadir angles, θ and with the same solid angle at the detector,

$$d\Omega = dS' \cos \theta' / (d')^2 = dS'' \cos \theta'' / (d'')^2. \quad (15)$$

The distance to the patch above the horizon is $d' = \ell$ and the distance to the

patch below the horizon is d'' , while the local zenith angles at the patches are θ' and θ'' . By a geometrical construction one can show that the angles are related by

$$\cos \theta' = \cos \theta'' = \sqrt{1 - (r_A/r_S)^2 \sin^2 \theta} \geq \sqrt{1 - (r_A/r_S)^2} \approx 0.07. \quad (16)$$

Next let $Y_{\nu_i}(E_\nu, \Omega') dE_\nu dS' d\Omega'$ be the number of neutrinos of type i emitted from the patch dS' in energy interval $[E_\nu, E_\nu + dE]$ into the solid angle $d\Omega' = d \cos \theta' d\varphi'$ centered at $\Omega' = (\cos \theta', \varphi')$, per unit time. We represent the projected area of the detector as a function of zenith angle as $\mathcal{A}(\theta)$. Then, if the detector is up-down symmetric (i.e. $\mathcal{A}(\theta) = \mathcal{A}(180^\circ - \theta)$), the solid angle subtended by the detector is $\mathcal{A}/(d')^2$ above the horizon and $\mathcal{A}/(d'')^2$ below. The corresponding rates of neutrinos through the detector are $Y_{\nu_i}(E_\nu, \Omega') dE_\nu dS' \times \mathcal{A}/(d')^2$ and $Y_{\nu_i}(E_\nu, \Omega'') dE_\nu dS'' \times \mathcal{A}/(d'')^2$ respectively. The differential rate from the patch above the horizon is

$$\frac{dN_{\nu_i}}{dE_\nu d\Omega d\mathcal{A}} = \frac{Y_{\nu_i}(E_\nu, \Omega') dE_\nu dS' \times (\mathcal{A}/(d')^2)}{dE_\nu (dS' \cos \theta' / (d')^2) (\mathcal{A})} = \frac{1}{\cos \theta'} Y_{\nu_i}(E_\nu, \Omega') \quad (17)$$

with the same result for the patch below the horizon. Eq. 15 has been used for $d\Omega$. Since the distances cancel and $\theta'' = \theta'$, the flux is symmetric from above and below the horizon no matter how complicated the dependence of Y_ν on angle, provided it is the same above and below the horizon (i.e. in the absence of geomagnetic effects, mountains, seasonal variations, etc.). To the extent that the detector response is also symmetric, the measured rates will be as well. The factor $1/\cos \theta'$ in Eq. 17 is the origin of the enhancement near the horizontal in the 3D calculation. It comes from the expression 15 for the solid angle of the production region, and it is limited by the inequality in Eq. 16.

The relation between the yield for a patch of the production shell and the

incident cosmic-ray flux is

$$Y_{\nu_i}(E_\nu, \Omega') = \int_{E_{cr}} \int_{\Omega_{cr}} [\eta_{\nu_i}(E_\nu, \Omega' : E_{cr}, \Omega_{cr})] \times [(dN_{cr}/dE_{cr}) \cos \theta_{cr}] d\Omega_{cr} dE_{cr}, \quad (18)$$

where $\eta_{\nu_i}(E_\nu, \Omega' : E_{cr}, \Omega_{cr})$ is the differential probability with which primary cosmic rays with energy E_{cr} and arrival direction $\Omega_{cr} = (\cos \theta_{cr}, \varphi_{cr})$ produce ν_i in the energy interval $[E_\nu, E_\nu + dE]$ and solid angle $d\Omega'$. Apart from geomagnetic effects the flux of cosmic rays, dN_{cr}/dE_{cr} ($\text{cm}^2 \cdot \text{sr} \cdot \text{s} \cdot \text{GeV}$) $^{-1}$, is isotropic. The factor $\cos \theta_{cr}$ in Eq. 18 is the projection of the isotropic flux onto the surface element dS' that is needed to obtain the rate at which primaries enter the production shell from a particular arrival direction.

As energy increases neutrino production becomes peaked in the forward direction ($\cos \theta_{cr} = \cos \theta'$). In the high energy limit $\eta_{\nu_i}(E_\nu, \Omega') \rightarrow \eta_{\nu_i}(E_\nu, \cos \theta') \times \delta(\Omega', \Omega_{cr})$, and we recover the one-dimensional approximation. Then $Y_{\nu_i}(E_\nu, \Omega') \propto \cos \theta'$ and the horizontal enhancement in Eq. 17 is exactly canceled. For low energy neutrinos the deviation from the direction of the parent primary cannot be neglected and the cancellation is not complete. Eq. 14 sets the energy scale for the horizontal enhancement.

We return now to a discussion of the results displayed in Fig. 20. The intrinsic angular dependence of the one-dimensional calculation in the absence of the geomagnetic field is displayed in the left panel Fig. 3 in §2.1. When geomagnetic effects are unimportant, there is an excess of neutrinos near the horizon. At Super-K, however, there are regions of very high cutoff rigidity near the horizon, which leads to the suppression of low-energy neutrinos from near $\cos \theta = 0$ for the 1D calculation shown by the line histograms in Fig. 20. The characteristic peaking near the horizon only appears again at Super-K for $E_\nu > 1$ GeV (panel d

in the figure). At this energy the three-dimensional effects are also negligible, and the 1D and 3D calculations agree. At lower energy, however, the flat behavior or suppression near $\cos \theta \sim 0$ is replaced with the horizontal peak characteristic of the correct 3D treatment.

The horizontal enhancement of the neutrino flux appears mainly at low energy and is therefore essentially impossible to detect because of the large angle between a low energy neutrino and the charged lepton that it produces in the detector (34). The enhancement is significant only for lower energies and for $|\cos(\text{zenith})| \approx 0.2$, within 12 degrees from the horizontal direction. Since the angle between the neutrino and the charged lepton it produces in the detector is expected to be ~ 60 degree below 0.5 GeV, the horizontal enhancement cannot be resolved.

7.2 Pathlength distributions

A key element of the interpretation of the evidence for oscillations is the pathlength-dependence of the atmospheric neutrino beam. To a first approximation, the distribution is a delta function equal to the distance from the detector along the direction of the neutrino to a shell at approximately 15 kilometers altitude. The next step was to calculate the pathlength distribution corresponding to the distribution of production depths still assuming the neutrino is along the direction of the primary cosmic ray that produced it (116). This is the approach used so far in the analysis of the Super-K data, and the mean value of the pathlength in the 1D calculation (116) is shown in Fig. 22a. What is still lacking is a treatment of the pathlength distribution with the full three-dimensional geometry. In particular, the excess of low energy neutrinos near the horizon in the 3D calculation arises in part from neutrinos produced closer to the detector than neutrinos

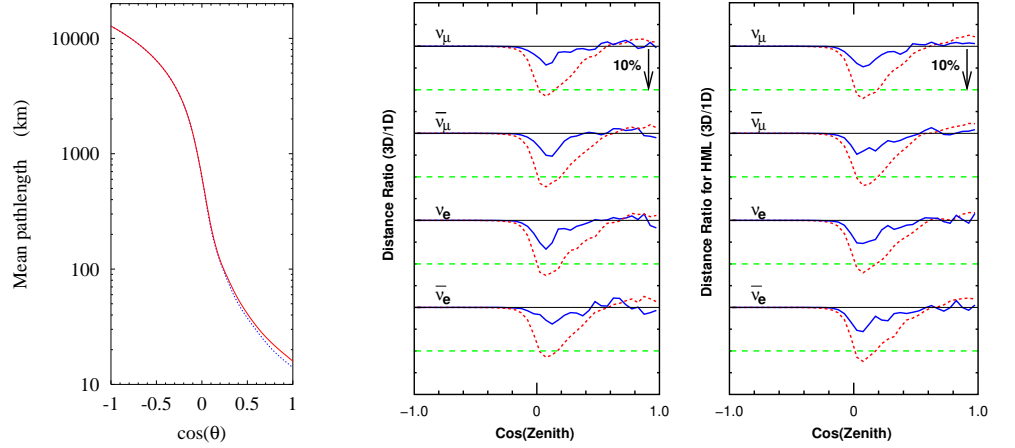


Figure 22: a) Mean pathlength of neutrinos with $0.3 < E_\nu < 2$ GeV in a 1D calculation (116). b) Ratio of the median path length in 3D calculation to that in 1D calculation both for Super-K and North America. Solid lines show the ratio for 1 GeV neutrinos, and dotted lines for 0.3 GeV neutrinos. $\cos \theta = 1$ denotes the downward direction for neutrinos.

from the same direction in the 1D calculation. This is possible because the more nearly vertical nearby primaries can contribute neutrinos at zenith angles that would require larger pathlengths if the primary and the neutrino direction were the same. The nearby case just described is not fully compensated by larger angle primaries producing smaller angle neutrinos. This is a consequence of the $\cos \theta_{cr}$ projection factor in Eq. 18.

We compare the path length calculated in the 1D and 3D calculations, converting the median production height to the path length by a simple relation:

$$\ell = \sqrt{(h^2 + 2R_\oplus h) + (R_\oplus \cos \theta)^2} - R_\oplus \cos \theta \quad . \quad (19)$$

We show the ratio of the two path lengths (3D/1D) as a function of $\cos(\theta)$ in Fig. 22 from Ref. (88). In this comparison an average over azimuth has been made. Near the horizon the production distance of 0.3 GeV neutrinos is $\sim 10\%$

smaller for 3D calculation than for 1D. For 1 GeV the difference decreases to $\lesssim 5\%$. As there is not a visible difference between the plots for Kamioka and for high-latitude North America, we may conclude that there is almost no geomagnetic latitude dependence of the path length differences.

8 Atmospheric muons

In this section we review the use of muon flux as a constraint on the atmospheric neutrino calculations. We focus on the low energy region, where pions give the dominant contribution to neutrinos as well as to muons.

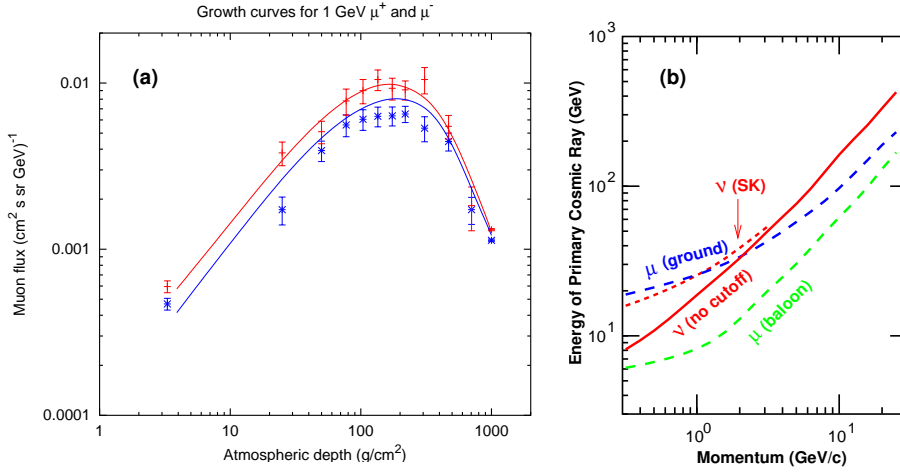


Figure 23: a. Growth curve of muons. The data are those of Ref. (117) and lines are 3D calculations from Ref. (118). b. Median primary energy per nucleon for muons and neutrinos (see text).

Fig. 23a shows the growth curve of the vertical atmospheric muon flux for $E_\mu \approx 1$ GeV as a function of atmospheric depth X (gm/cm^2). The flux increases with depth from top of atmosphere down to $X \sim 100 \text{ g/cm}^2$. For $X \ll \lambda_N \approx 80 \text{ gm/cm}^2$ (where λ_N is the nucleon interaction length) the increase is proportional to X . In the region of 100–200 g/cm^2 , the attenuation of

the primary cosmic rays and the increase of the column density compensate each other, and the muon flux is almost constant. Below 200 g/cm^2 , the muon flux decreases rapidly as muon production decreases and muon decay and energy-loss become important. Since decay probability and the importance of energy loss depend on energy, the growth curve depend somewhat on energy, but the qualitative behavior is unchanged.

Fig. 23b shows the median primary energy per nucleon for vertical muons (dashed lines) and neutrinos averaged over all angles (heavy solid and dotted curves). Comparison of response curves for muons at the ground and at float altitude (typically $< 5 \text{ g/cm}^2$) shows the effect of muon energy loss in the atmosphere. Muons typically lose $\approx 1.8 \text{ GeV}$ propagating through the atmosphere, and most muons produced with this energy decay before reaching the ground. On the other hand, high in the atmosphere the muons have not lost energy and are closer in energy to the primaries. For neutrinos, the solid line is for Kamioka site, and the dotted line is the result that would be obtained in the absence of a geomagnetic cutoff. The response curve for north America or Gransasso would be between the solid and dashed lines. Both muon charges (μ^+, μ^-), and all neutrinos species ($\nu_\mu, \bar{\nu}_\mu, \nu_e, \bar{\nu}_e$) were summed for these curves.

Measurements of muons in the cosmic radiation date back to the early days of the subject. A wealth of information on this and other relevant topics is to be found in the comprehensive work of Grieder (119). There is also a recent study of muons with $E \gtrsim 10 \text{ GeV}$ at ground level in which the authors have corrected the data for different observing conditions (120). A thorough summary is also given in Ref. (121). In the past decade, several groups have measured the flux of muons on the ground and during ascent to float altitude (50, 117, 122, 123), and

several groups (36, 112, 114, 118, 125) have compared their calculations to some or all of this data.

Several issues arise in comparing calculations with muon data. One is whether to use the primary spectrum measured during the muon flight (if available) or to use some kind of best fit or preferred spectrum. For example, Battistoni et al. (125) get generally good agreement with the Caprice muon data (117) using the primary spectrum of Ref. (32), which is higher than that measured the Caprice detector (51) at the same time as the muon measurement was made. They note that their normalization would have been generally lower than the muon data had they used the Caprice primary spectrum. On the other hand the CAPRICE primary spectrum is used in Ref. (118) to obtain the results shown in Fig. refFig-mu-growtha. That calculation uses the interaction model Target 2.1, which gives higher neutrino fluxes at Soudan than the calculation with FLUKA (34). Since the muon fluxes are also measured with no geomagnetic cutoff, the origin of the difference between these two results is presumably the same—a difference in pion production in interactions of $E_N < 10$ GeV.

Fig. 24 (36) compares calculations with data of two measurements both made in summer at Lynn Lake in Northern Canada where the geomagnetic cutoff is negligible. The Caprice muon data (117, 126) was obtained in 1994, while the BESS muon data is a compilation of observations made in 1997, 1998, and 1999 (123, 124). The neutron monitor count rates for both experiments (averaged over the three dates in the case of BESS) are similar to that of 1998 when BESS and AMS measured the primary cosmic ray spectrum (see Fig. 8). The left panel shows a comparison with the muon fluxes at the ground. The comparison at float altitude is shown on the right. It is noteworthy that the two measurements

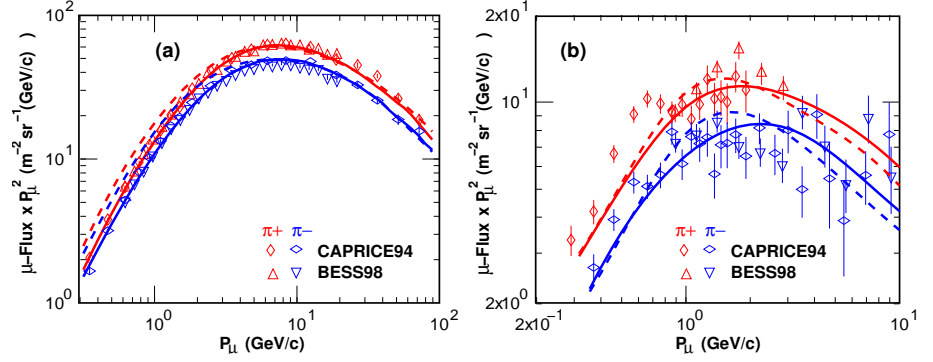


Figure 24: The flux of positive and negative muons observed at Lynnlake and corresponding calculations. Left panel refers to measurements at the ground (126, 124); right panel to float altitude (117, 123). Thick solid and dotted lines show the positive and negative pion spectra calculated based on Dpmjet3 interaction model (36). Thin solid and dotted lines show the positive and negative pion spectra calculated based on Fritiof 1.6 interaction model as used in (35).

of the muon flux at the ground are in better agreement with each other than the corresponding two measurements of the primary proton spectrum (51, 53). Despite relatively long exposures at float altitude, the statistics are poor because of the low flux.

Finally, we note that it may also be useful to compare high-statistics ground level measurements made at different geomagnetic locations. Ref. (126) compares a measurement at Lynn Lake ($R_c \approx 0.5$ GV) with one at Ft. Sumner ($R_c \approx 4.2$ GV). Ref. (124) compares their ground level measurement at Lynn Lake with a measurement at Tsukuba, Japan, which has a higher cutoff of 11.4 GV. The charge ratios measured at the locations with a significant geomagnetic cutoff fall below those measured at Lynn Lake for $E_\mu < 1$ GeV. This is expected qualitatively for several reasons. Helium is relatively more important at high cutoff because the energy per nucleon at cutoff is approximately half that of protons,

and helium produces a charge ratio of unity. In addition, when the cutoff is high the low energy muons must come more from the central region of interactions above cutoff, and the charge ratio is lower in the central region. Finally, there is also some contribution from the east-west effect since vertical muons of opposite sign are bent in opposite directions (127).

We summarize this section as follows. Because of decay and energy loss, low energy muons at the ground carry less information about neutrino production than those at high altitude where most of the neutrinos are produced. In addition, the variation of atmospheric structure from barometric and seasonal changes is significant and must be accounted for. At float altitude, the muons reflect rather directly the properties of pion production and primary cosmic-ray intensity since only one interaction is involved, but this is above the depth where most muons and neutrinos are produced and the flux is very low. On the other hand, the peak of the grown curve has so far been studied only during ascent where the balloon rises rapidly through the atmosphere, so that statistical and systematic uncertainties are larger than on the ground or at float. In addition, at all altitudes, the fraction of $\sim\text{GeV}$ muons passing through a detector is always much smaller than the number of muons that were produced above it (118). Thus calculating the muon flux is more delicate than calculating the neutrino flux which is an integral over all depths.

9 Uncertainties in the Calculated Neutrino Fluxes

Remaining uncertainties in the flux of atmospheric neutrinos come mainly from the primary spectrum and from the treatment of hadronic interactions. In addition, there remain uncertainties of a technical nature related to remaining ap-

proximations in present calculations. The uncertainty in the signal for a given experiment depends on its response function, which determines the distribution of primary energy responsible for the signal. Key examples are shown in Fig. 5.

9.1 *Uncertainties from primary spectrum*

An estimate (60) of the uncertainty in the primary spectrum in the light of recent measurements by BESS (53) and AMS (54) is $\pm 5\%$ below 100 GeV/nucleon increasing to $\pm 10\%$ at 10 TeV/nucleon. This is based on a fit (Eq. 10 to BESS and AMS data alone and assumes a power-law to extrapolate beyond the upper range of those measurements (≈ 100 GeV).

A more proper estimate of the uncertainty in the primary spectrum uses all valid measurements, including those with larger quoted uncertainties, to estimate the systematic uncertainty in the primary spectrum. Fig. 6 shows a collection of measurements for protons and helium. Although there are now several recently reported measurements below 100 GeV, there is a striking lack of recent data in the TeV range, important for ν -induced upward muons. Even assuming the high-energy data should be renormalized down to connect with the low-energy data, the measurements cover a range of $\pm 20\%$ below 100 GeV and $\pm 30\%$ above.

9.2 *Uncertainties from hadronic interactions*

It is more difficult to quantify the uncertainties due to hadronic interactions. As shown in Fig. 16, large regions of phase space are not measured, and models are needed to interpolate and extrapolate into the unmeasured regions. Study of Fig. 15 show a scatter of 20-25% even if we consider the data of Ref. (98) as an outlier. On the other hand, this treats the different inclusive cross sec-

tions as independent of each other, when in fact they are interrelated by energy conservation.

Combining the systematic uncertainties in primary spectrum and in pion production as if they were independent statistical uncertainties, we would therefore estimate an overall theoretical uncertainty of ± 20 to 25% in the energy range relevant for contained neutrino interactions and somewhat larger at higher energy.

9.3 Other sources of uncertainty

Calculations usually assume a spherical earth with the surface at sea level. When parent mesons enter the ground before decaying they lose energy rapidly by ionization or the nuclear interactions and produce only very low energy neutrinos. Therefore, when there is a high mountain over the neutrino detector, the neutrino flux is reduced to some extent. The effect is negligible except near the vertical and then only for decay products of muons. The reduction has been estimated (128) as a 2-3 % effect for ν_e in the 10-100 GeV range due to the Ikenoyama mountain over Super-Kamiokande, which has a peak at approximately 1300 m above sea level.

Calculations are normally made for an average atmosphere. While pressure and seasonal variations have a noticeable effect on surviving muon fluxes at the ground, they are small for neutrinos. Variations at the per cent level have been estimated in Ref. (128).

9.4 Comparison to measurements

A consistent picture emerges from comparison of a variety of data to calculations of the flux of atmospheric neutrinos. All analyses emphasize compari-

son to ratios, which include ν_e/ν_μ and up/down for contained events and stopping/throughgoing and vertical/horizontal for neutrino-induced upward muon. As a consequence, an offset in normalization does not affect the conclusions about oscillations, which are robust.

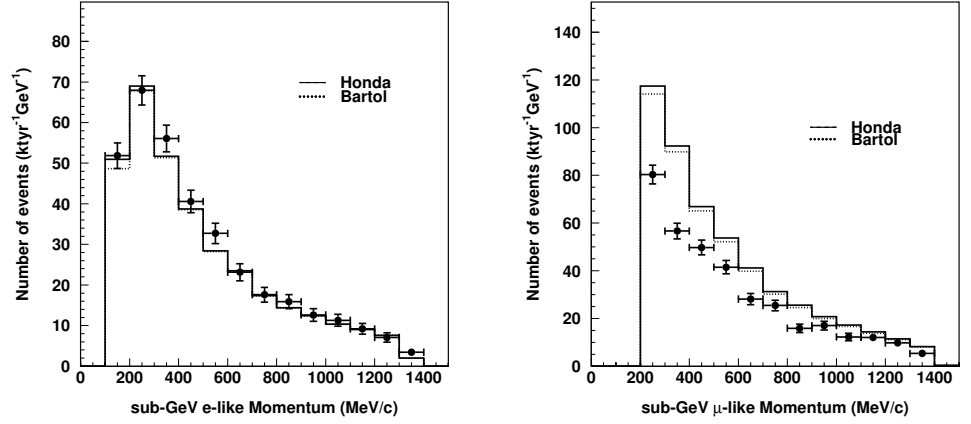


Figure 25: Sub-GeV neutrino spectrum.

Nevertheless, it is also interesting and informative to compare the measured neutrino flux as directly as possible in an absolute fashion with the calculations. Fig. 25 compares the neutrino fluxes measured at Super-K with the two calculations (35, 32) that have been used extensively as input to the detector simulation. The comparisons are made as a function of visible energy by the Super-K group (129). The magnitudes are consistent with what is expected for oscillations in this energy range that involve ν_μ and ν_τ but not ν_e ; namely, there is a deficit of ν_μ , whereas the measured flux of electron neutrinos is consistent with the calculation.

Systematic comparisons of more recent calculations with data are not yet available. Based on comparisons between old and new calculations such as those shown in Fig. 19, however, we expect that the new calculations will give significantly

lower predicted neutrino fluxes. In Refs. (33, 100) this will be a consequence of lower pion production, whereas in the case of Ref. (36) the primary spectrum is lower than before (35). We expect the predictions may be reduced by as much as 15 to 20%, without changing the ratios significantly. Possible resolutions include uncertainties in the neutrino cross sections (130, 131) or systematic uncertainty in primary spectrum (despite the agreement between BESS (53) and AMS (54) or higher pion production (despite new calculations) or some combination of the above.

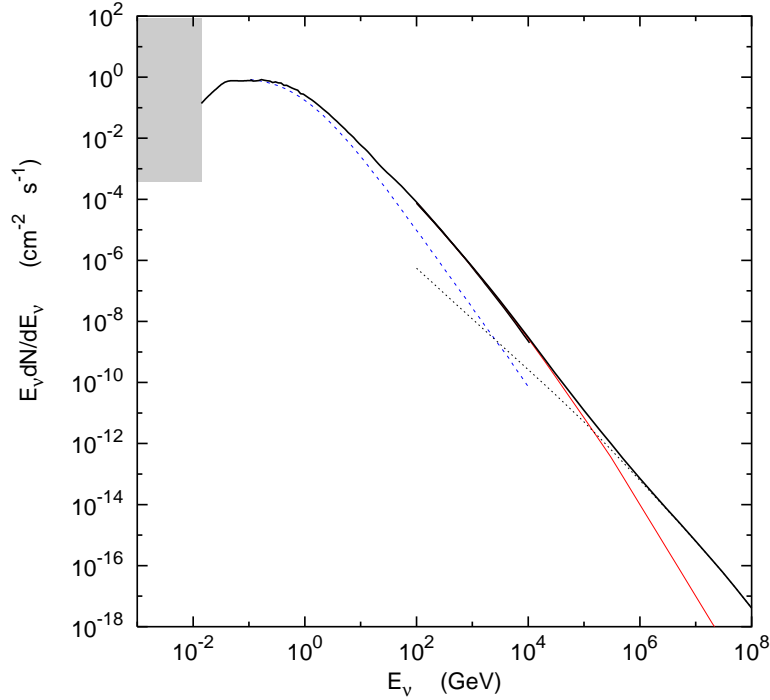


Figure 26: Global view of the neutrino spectrum: vertical flux of $\nu_\mu + \bar{\nu}$ (heavy solid line); $\nu_e + \bar{\nu}_e$ (dashed line); prompt neutrinos (dotted line); $\nu_\mu + \bar{\nu}$ from pions and kaons (thin solid line at high energy).

10 Global view of the neutrino spectrum

Figure 26 is a global view of the omnidirectional neutrino flux from the MeV range up to 100 PeV. Below 15-18 MeV solar neutrinos dominate, as indicated by the shaded region. It has been pointed out (132, 133, 134) that there is potentially a window between ~ 15 and 50 MeV where the accumulated diffuse flux from supernovae in the Universe could be comparable to or larger than the flux of atmospheric neutrinos.

The heavy solid line shows the flux of atmospheric $\nu_\mu + \bar{\nu}_\mu$ integrated over all directions. The dotted lines show the flux of $\nu_e + \bar{\nu}_e$. Where geomagnetic effects are important (below several GeV), we show the integrated flux at Kamioka. With the discovery of oscillations, the flux of muon neutrinos is suppressed in the energy region below 100 GeV. We used the Super-K oscillation parameters (6) assuming $\nu_\mu \leftrightarrow \nu_\tau$ to relate the production spectrum of $\nu_\mu + \bar{\nu}_\mu$ as calculated in Ref. (32) to the flux at the detector. Thus for $E_\nu < 10$ GeV the ν_μ/ν_e ratio decreases toward 1.

For $E_\nu \sim 100$ GeV and beyond, most neutrinos come from decay of kaons until the energy is so high that prompt neutrinos dominate. The dotted line at higher energy is the flux of prompt neutrinos ($\nu_e + \bar{\nu}_e \approx \nu_\mu + \bar{\nu}_\mu$) from decay of charm, as estimated in the RQP model of Ref. (110). In this model, the charm crossover is at ~ 3 TeV for electron neutrinos and around 100 TeV for muon neutrinos. The thinner (lower) solid line above 100 TeV is the non-prompt contribution to the flux of $\nu_\mu + \bar{\nu}_\mu$. In the TeV region and above the atmospheric neutrinos become a foreground for high energy astrophysical neutrinos, and the uncertainty in the level of prompt neutrinos becomes an important consideration in this context.

11 Acknowledgments

We are grateful to Giles Barr, Giuseppe Battistoni, Ralph Engel, Frank Jones, T. Kajita, K. Kasahara, Paolo Lipari, S. Midorikawa, Teresa Montaruli, T. Sanuki and Todor Stanev for their assistance and advice as we prepared this review. The data plotted in Fig. 8 are from research supported by National Science Foundation Grant ATM-9912341 at the University of Chicago. One of us (TKG) gratefully acknowledges the hospitality of the Institute for Cosmic Ray Research where most of this review was prepared. The work of TKG is supported in part by the U.S. Department of Energy under DE-FG02 91ER 40626.

12 LITERATURE CITED

References

1. Markov MA, in *Proc. 1960 Annual Int. Conf. on High Energy Physics at Rochester* (ed. Sudarshan ECG, Tinlot JH, & Melissinos AC.) p578 (1960)
2. Markov MA, Zheleznykh IM. *Nuclear Physics* 27:385 (1961)
3. Greisen K, *Ann. Rev. Nucl. Science* 10:63 (1960)
4. Achar CV, et al. *Phys. Lett.* 18:196 and 19:78 (1965)
5. Reines F, et al. *Phys. Rev. Lett.* 15:429 (1965)
6. Fukuda Y, et al. *Phys. Rev. Lett.* 81:1562 (1998)
7. Fukuda S, et al. *Phys. Rev. Lett.* 85:3999. (2000)
8. Ahmad QR, et al. *Phys. Rev. Lett.* 87:071301 (2001)
9. Haines TJ, et al. *Phys. Rev. Lett.* 57:1986 (1986)
10. Hirata KS, et al. *Phys. Lett.* B205:416 (1988)

11. Berger Ch, et al. *Phys. Lett.* B245:305 (1990)
12. Casper D, et al. *Phys. Rev. Lett.* 66:2561 (1991)
13. Becker-Szendy R, et al. *Phys. Rev.* D46:3720 (1992)
14. Hirata KS, et al. *Phys. Lett.* B280:146 (1992)
15. Beier EW, et al. *Phys. Letters* B283:446 (1992)
16. Allison WWM, et al. *Phys. Lett.* B391:491 (1997) and B449:137 (1999)
17. Fukuda Y, et al. *Phys. Lett.* B335 (1994) 237.
18. Lipari P. in *Neutrino Oscillations and their Origin* (ed. Suzuki Y, Nakahata M, Shiozawa M, & Kaneyuki K. Universal Academy Press, 2000) p. 65
19. Ambrosio M, et al. *Phys. Lett.* B517:59 (2001) and B434:451 (1998)
20. Fukuda Y, et al. *Phys. Rev. Lett.* 82:2644 (1999)
21. Ambrosio M, et al. *Phys. Lett.* B478:5 (2000)
22. Fukuda Y, et al. *Phys. Lett.* B467:185 (1999)
23. Kajita T, Totsuka Y. *Revs. Mod. Phys.* 73:85 (2001)
24. Jung C-K, Kajita T, Mann A, McGrew C, *Ann. Revs. Nucl. Part. Sci.* 51:451 (2001)
25. Balkanov VA, et al. *Nucl. Phys. B Proc. Suppl.* 91:438 (2001)
26. Andres E, et al. *Astropart. Phys.* 13:1 (2000)
27. Bottai S, et al. *Nucl. Phys. B Proc. Suppl.* 85:153 (2000)
28. Thompson LF, et al. *Nucl. Phys. B Proc. Suppl.* 91:431 (2001)
29. <http://nemoweb.lns.infn.it/>
30. Goldschmidt A, et al. *Proc. 27th Int. Cosmic Ray Conf.* 3:1237 (2001)

31. Zatsepin GT, Kuz'min VA. *Soviet Phys. JETP* 14:1294 (1961)
32. Agrawal V, Gaisser TK, Lipari P, & Stanev T. *Phys. Rev* D53:1314 (1996)
33. Engel R, Gaisser TK, Lipari P, & Stanev T, *Proc. 27th Int. Cosmic Ray Conf.* 4:1381 (2001)
34. Battistoni G, et al. *Astropart. Phys.* 12:315 (2000) and [http://www. mi. infn. it/ battist/neutrino. html](http://www.mi.infn.it/battist/neutrino.html)
35. Honda M, Kajita T, Kasahara K, & Midorikawa S. *Phys. Rev.* D52:4985 (1995)
36. Honda M, Kajita T, Kasahara K, & Midorikawa S. *Proc. 27th Int. Cosmic Ray Conf.* 3:1162 (2001)
37. Volkova LV. private communication (1988)
38. Zatsepin GT, Kuz'min VA. *Soviet Phys. JETP* 12:1171 (1961)
39. Perkins DH. *Nucl. Phys.* B399:3 (1993)
40. Perkins DH. *Astropart. Phys.* 2:249 (1994)
41. Gaisser, TK. *Cosmic Rays and Particle Physics* (Cambridge University Press, 1992)
42. Lipari P. *Astropart. Phys.* 1:195 (1993)
43. Gaisser TK. *Astropart. Phys.* 16:285 (2002)
44. Compton AH, Getting IA. *Phys. Rev.* 47:817 (1935)
45. Cutler DJ, Groom DE. *Astrophys. J.* 376:322 (1991)
46. Nagashima K, Fujimoto K, Jacklyn RM. *J. Geophys. Res.* 103:17429 (1988)
47. Webber WR, Golden RL, Stephens SA. *Proc. 20th Int. Cosmic Ray Conf.* 1:325 (1987)

48. Seo E-S, et al. *Astrophys. J.* 378:763 (1991)
49. Pappini P, et al. *Proc. 23rd Int. Cosmic Ray Conf.* 1:579 (1993)
50. Bellotti R, et al. *Phys. Rev.* D60:052002 (1999)
51. Boezio M, et al. *Astrophys. J.* 518:457 (1999)
52. Menn W, et al. *Astrophys. J.* 533:281 (2000)
53. Sanuki T, et al. *Astrophys. J.* 545:1135 (2000)
54. Alcarez J, et al. *Phys. Lett.* B490:27 (2000)
55. Ryan MJ, Ormes JF, Balasubrahmanyam VK. *Phys. Rev. Lett.* 28:985, E1497 (1972)
56. Asakamori K, et al. *Ap. J.* 502:278 (1998)
57. Ivanenko IP, et al. *Proc. 23rd Int. Cosmic Ray Conf.* 2:17 (1993)
58. Apanasenko AV, et al. *Astropart. Phys.* 16:13 (2001)
59. Kawamura Y, et al. *Phys. Rev.* D40:729 (1989) (1989)
60. T. K. Gaisser, M. Honda, P. Lipari & T. Stanev, *Proc. 27th Int. Cosmic Ray Conf.* (2001) 1643.
61. Stanev T. Private communication.
62. *The Heliosphere at Solar Minimum* (ed. Page DE, Marsden RG,) Pergamon Press, (1997)
63. Simpson J. *Phys. Rev* 73:1389 (1948)
64. Clem JM, Dorman LI. *Space Science Reviews* 93:335 (2000)
65. <http://www.bartol.udel.edu/neutronm/>
66. <http://ulysses.uchicago.edu/NeutronMonitor/Misc/neutron2.html>
67. Nagashima K, et al. *Nuovo Comento* C12:173 (1989)

68. Lipari P. private communication (2001)
69. Gleeson LJ, Axford WI. *Astrophys. J.* 154:1011 (1968)
70. Asaoka Y, et al. *Phys. Rev. Letters* 88:51101 (2002)
71. Störmer C. *Z. Astrophys.* 1:237 (1930)
72. Alpher RA. *J. Geophys. Res.* 55:437 (1950)
73. <http://nssdc.gsfc.nasa.gov/space/model/models/igrf.html>
74. Lipari P, Stanev T. *Proc. 24th Int. Cosmic Ray Conf.* 1:516 (516)
75. Johnson TH, *Phys. Rev.* 43:834 (1933)
76. Alvarez LW, & Compton A. H. *Phys. Rev.* 43:835 (1933)
77. Futagami T, et al. *Phys. Rev. Lett.* 82:5192 (1999)
78. Lipari P, Stanev T & Gaisser TK, *Phys. Rev.* D58:073003 (1998)
79. Lipari P. *Astropart. Phys.* 14:153 (2000)
80. Alcarez J, et al. *Phys. Lett.* B472:215 (2000)
81. Treiman SB. *Phys. Rev.* 53:957 (1953)
82. Barwick SW, et al. *J. Geophys. Res.* 103:4817 (1998)
83. Verma SD, *J. Geophys. Res.* 72:915 (1967)
84. Derome L, et al. *Phys. Lett.* B489:1 (2000)
85. Lipari P. *Astropart. Phys.* 16:295 (2002)
86. Zuccon P, et al. astro-ph/0111111
87. Lipari P, *Astropart. Phys.* 14:171 (2000)
88. Honda M, Kajita T, Kasahara K, Midorikawa S. *Phys. Rev.* D64:053011 (2001)

89. Ralph Engel, private communication.
90. Glauber RJ, Matthiae G. *Nucl. Phys.* B21:135 (1970)
91. Dersch U, et al. *Nucl. Phys. B* 579:277 (2000)
92. Engel J, Gaisser TK, Lipari P, Stanev T. *Phys. Rev.* D46:5013 (1992)
93. Cho Y, et al. *Phys. Rev.* D4:1967 (1971)
94. Sanford JR, Wang CL. BNL, AGS internal report (unpublished, 1967); Wang, CL. *Phys. Rev. Lett.* 25:1068, 1536(E) (1970)
95. Allaby JV, et al. CERN Yellow Report 70-12 (1970)
96. Eichten T, et al. *Nucl. Phys.* B44:333 (1972)
97. Abbott T, et al. *Phys. Rev.* D45:3906 (1992)
98. Lundy RA, et al. *Phys. Rev. Lett.* 14:504 (1965)
99. Engel R, Gaisser TK, & Stanev T, *Phys. Lett.* B472:113 (2000)
100. Ferrari A. *Physica Medica* Vol. XVII, Suppl. 1.
101. G. Battistoni, private communication.
102. Roesler S, Engel & R, Ranft J. *Proc. 27th Int. Cosmic Ray Conf.* 1:439 (2001), *Phys. Rev.* D57:2889 (1998), D55:6957 (1997)
103. Nilsson-Almqvist & B, Stenlund E. *Comput. Commun.* 43:387 (1987)
104. Tan LC, & Ng LK. *J. Phys. G: Nucl. Phys.* 9:1453 (1983)
105. Costa CGS. *Astropart. Phys.* 16:193 (2001)
106. Volkova LV, Fulgione W, Galeotti P, & Saavedra O. *Nuovo Cimento* C10:465 (1987)
107. Thunman M, Ingelman G, & Gondolo P. *Astropart. Phys.* 5:309 (1996)
108. Pasquali L, Reno MH, & Sarcevic I. *Phys. Rev.* D59:034020 (1999)

109. Gaisser TK, & Halzen F. *Phys. Rev.* D11:3157 (1973)
110. Bugaev EV, et al. *Phys. Rev.* D58:054001 (1998)
111. Tserkovnyak Y, Komar RJ, Nally CW, & Waltham CE. *Proc. 27th Int. Cosmic Ray Conf.* 3:1196 (2001)
112. Fiorentini G, Naumov VA, & Villante FL. *Phys. Lett.* B510:173 (2001) and *Proc. 27th Int. Cosmic Ray Conf.* 3:1218 (2001)
113. Wentz J, et al. *Proc. 27th Int. Cosmic Ray Conf.* 3:1167 (2001) and private communication
114. Liu Y, Derome L. & Buénerd M, *Proc. 27th Int. Cosmic Ray Conf.* 3:1033. (2001)
115. Plyaskin V, *Phys. Lett.* B516:213 (2001)
116. Gaisser TK, & Stanev T. *Phys. Rev.* D57:1977 (1998)
117. Boezio M, et al. *Phys. Rev.* D62:032007 (2000)
118. Engel R, Gaisser TK, & Stanev T. *Proc. 27th Int. Cosmic Ray Conf.* 3:1029 (2001)
119. Grieder PKF. Cosmic Rays at Earth, Researcher's Reference Manual and Data Book (Elsevier Science, 2001)
120. Hebbeker T, & Timmermans C. *Astropart. Phys.* (to be published, hep-ph/0102042)
121. Naumov VA. hep-ph/0201310
122. Coutu S, et al. *Phys. Rev.* D62:032001 (2000)
123. Sanuki T, et al. *Proc. 27th Int. Cosmic Ray Conf.* 3:950 (2001)
124. Motoki M, et al. *Proc. 27th Int. Cosmic Ray Conf.* 3:927 (2001)

125. Battistoni G, Ferrari A, Montaruli T, & Sala PR. *Astropart. Phys.* (to be published; hep-ph/0107241)
126. Kremer J, et al. *Phys. Rev. Lett.* 83:4241 (1999)
127. Stanev T, Coutu S, Gaisser TK, & Barr G. *Proc. 26th Int. Cosmic Ray Conf.* 2:96 (1999)
128. Honda M. *Neutrino Oscillation and their origin*, Universal Academy Press (ed. Suzuki Y, Nakahata M, Shiozawa M, & Kaneyuki K. Universal Academy
129. Kajita T. Private communication
130. Lipari P, Lusignolo M, Sartogo F. *Phys. Rev. Letters* 74:4384 (1995)
131. *Proc. Workshop on Neutrino-Nucleus Interactions in the Few GeV Region*, *Nucl. Phys. B (Proc. Suppl)* (to be published, 2000)
<http://neutrino.kek.jp/nuint01/> December 2001
132. Krauss LM, Glashow SL, Schramm DN. *Nature* 310:191 (1984)
133. Bisnovaty-Kogan GS, Seidov SF. *Ann NY Acad. Sci* 422:319 (1984)
134. Totani T, Sato K, Yoshii Y. *Ap. J* 460:303 (1996)